

# On-Chip Generation of Vortical Flows for Microfluidic Centrifugation

Heba Ahmed, Shwathy Ramesan, Lillian Lee, Amgad R. Rezk,\* and Leslie Y. Yeo\*

Microcentrifugation constitutes an important part of the microfluidic toolkit in a similar way that centrifugation is crucial to many macroscopic procedures, given that micromixing, sample preconcentration, particle separation, component fractionation, and cell agglomeration are essential operations in small scale processes. Yet, the dominance of capillary and viscous effects, which typically tend to retard flow, over inertial and gravitational forces, which are often useful for actuating flows and hence centrifugation, at microscopic scales makes it difficult to generate rotational flows at these dimensions, let alone with sufficient vorticity to support efficient mixing, separation, concentration, or aggregation. Herein, the various technologies—both passive and active—that have been developed to date for vortex generation in microfluidic devices are reviewed. Various advantages or limitations associated with each are outlined, in addition to highlighting the challenges that need to be overcome for their incorporation into integrated microfluidic devices.

## 1. Introduction

The history of the centrifuge dates back to the discovery of centrifugal forces by the Dutch physicist and mathematician Christian Huygens (1629–1695) in 1659<sup>[1]</sup> and, subsequently, the development of a whirling arm drag-measuring apparatus by the English engineer Benjamin Robins (1707–1751), although it was not till 1864 that Antonin Prandtl (1842–1909), a German brewer, developed a design for separating cream from milk, to which turbines were added in 1877 by Swedish engineer Gustav De Laval (1845–1913), that the practical concept of a centrifuge was born. Since then, and the pioneering work of Theodor Svedburg (1884–1971), who received the Nobel Prize in Chemistry in 1926, centrifugation—and, more broadly, the generation of rotational flows from which centrifugal forces can be exploited—has been an indispensable process in the laboratory workflow, owing particularly to its use for particle separation and component fractionation. In the same way, microfluidic centrifugation, or microcentrifugation, is a critical operation in


lab-on-a-chip devices to facilitate on-chip micromixing, sample preconcentration, particle fractionation and sorting, component separation (e.g., the separation of red blood cells from plasma), and, cell trapping, lysis, and extraction, all of which constitute crucial sample preparation steps in the microfluidic drug discovery or point-of-care diagnostics workflow.<sup>[2–5]</sup>

Nevertheless, it is not straightforward to simply scale down a centrifuge, even if miniaturization of one was indeed possible, since sedimentation—the principle by which a centrifuge operates wherein particles separate under density gradients, is weak in microfluidic devices given the typically small particle Stokes numbers that are encountered, i.e.,  $Stk \equiv \rho_p d_p^2 U / 18\eta L \ll 1$ , wherein  $\rho_p$  and  $d_p$  is the particle density and diameter, respectively,  $U$  and  $L$  the characteristic

velocity and length scales of the system, and  $\eta$  the liquid viscosity. Consequently, the particle separation (or settling) time, which scales inversely to the Stokes number and the angular speed, is prohibitively long unless the rotational flow can be intensified. This, however, is not trivial given that typical Reynolds numbers  $Re \equiv \rho UL / \eta$  are also usually small in microfluidic devices ( $Re \lesssim 1$ ), owing to the small length scales, implying the dominance of viscous over inertial effects that highlight not only the difficulties in generating turbulent vortices but also the challenges in overcoming retardation of the flow due to viscous dissipation. While this can be remedied by massively increasing the flow rotation intensity with large pumps, for example, the use of such prohibits their integration onto the microfluidic device, and is therefore the antithesis of microfluidic philosophy, at least in its strictest sense, especially in the cases where complete miniaturization for portable, handheld functionality is desired.<sup>[3]</sup>

An exception to the above are inertial microfluidic systems<sup>[6,7]</sup> wherein geometry, topology, or curvature is introduced to the microchannel in order to generate the microscale recirculation or secondary Dean vortices required to drive on-chip microcentrifugation effects, although the large pressure drops encountered in these systems again necessitate considerable pumping capacity and the long channel lengths required for the separation render these systems typically challenging for miniaturization and integration. As such, inertial microfluidic systems have largely been developed to date for benchscale operations in the laboratory or the clinic, i.e., a chip-in-a-lab, as opposed to portable lab-on-a-chip systems for point-of-care

Dr. H. Ahmed, Dr. S. Ramesan, Dr. L. Lee, Dr. A. R. Rezk, Prof. L. Y. Yeo  
Micro/Nanophysics Research Laboratory  
School of Engineering  
RMIT University  
Melbourne, VIC 3000, Australia  
E-mail: amgad.rezk@rmit.edu.au; leslie.yeo@rmit.edu.au

 The ORCID identification number(s) for the author(s) of this article can be found under <https://doi.org/10.1002/sml.201903605>.

DOI: 10.1002/sml.201903605

applications. In any case, we discuss these systems in the context of strategies for passively generating recirculatory motion in microfluidic channels, but exclude the vast body of work exploiting these for inducing particle focusing and separation for a variety of applications, particularly circulating tumor cell isolation,<sup>[8,9]</sup> given that these have been the subject of a number of very comprehensive reviews (see, for example, refs. [6,7,10–12]).

A number of further points regarding the scope of the present review warrant clarification. We note that the term “microcentrifugation” historically has been associated with conventional centrifugation processes that are carried out in 0.2–2.0 mL microcentrifuge tubes and hence the use of “micro” in that context is somewhat a misnomer given that there is no significant scale associated with that process or setup that is particularly at microscale dimensions. Thus, even though the processes and devices we will describe below are truly microscale and hence could more accurately be referred to as “microcentrifugation” processes, we shall employ the terms “microfluidic centrifugation” or “on-chip microcentrifugation” in place to avoid confusion. We also exclude “centrifugal microfluidics” from the review since this is conceptually different to microfluidic centrifugation given that the primary rotation in these systems, also known as the “lab-on-a-CD,”<sup>[13]</sup> pertains to the motion of the discs themselves and is driven by a rotational motor, as opposed to the rotation of the fluid itself. While the spinning of these discs could induce the fluid within the microchannels patterned onto them to rotate, this is not necessarily true in all cases since the primary flow that is generated usually occurs in a linear, radially outward direction toward the periphery of the disc. Moreover, these have been the subject of a number of extensive reviews.<sup>[13–17]</sup> In addition, we also omit from the scope of this review technology that has been developed to date that allows rotation to be induced directly on particles and cells themselves (for example, that driven magnetically,<sup>[18]</sup> which, can also, in turn, be employed to drive vortical flows), as opposed to indirectly due to hydrodynamic rotation.

**Table 1** shows the different actuation mechanisms by which centrifugal flows can be generated in a microfluidic device. As with other microfluidic actuation schemes, on-chip centrifugation can be driven either passively, through the use of geometrical structures, or actively, by exploiting external forces.

## 2. Passive Actuation

### 2.1. Geometry

As was demonstrated in early work, the simplest way to generate vortical flows in a microfluidic device is to incorporate a side cavity, chamber, or notch into the microfluidic channel (see, for example, **Figure 1a** in which considerable hydrodynamic rotation within the cavity can be generated,<sup>[19]</sup> which can be exploited, for example, for particle separation due to density discrimination). Due to the sharp turn in the flow boundary, i.e., the channel wall, encountered at the corners associated with either of these features, the flow essentially expands and



**Leslie Y. Yeo** is a Distinguished Professor of Chemical Engineering at RMIT University, Melbourne. Following a Ph.D. from Imperial College London in 2002 and a postdoctoral stint at the University of Notre Dame, USA, he assumed faculty positions at Monash University and RMIT, where he held the Australian

Research Council's Australian Research Fellowship and Future Fellowship from 2009 to 2017.

detaches from the boundary, i.e., flow separation ensues, at which point the flow may no longer be viscous dominant and inertial effects could become increasingly apparent.<sup>[6]</sup> Concomitantly, the detachment of the flow from the boundary is accompanied by flow recirculation within the structure, although the emergence of such a vortical flow does not necessarily imply the existence of inertial effects.

In the example of a cavity, Yu et al.<sup>[21]</sup> reported that this occurs if the aspect ratio (transverse to longitudinal (with respect to the main flow axis) length scales) of the cavity is sufficiently large, or, if the reduced Reynolds number—the product of the aspect ratio squared and the hydrodynamic Reynolds number, independently exceeds a critical value. In other words, flow separation could occur for small reduced Reynolds numbers far below a value of unity if the cavity aspect ratio is sufficiently large, or for small aspect ratio cavities where the reduced Reynolds number is sufficiently large. In any case, the small vortex dimension  $R$ , which is defined by the size of the cavity, and the typically high rotational speeds  $V$  can lead to high radial accelerations on the order  $V^2/R$ , which for micrometer-dimension cavities, could reach  $10^6$ – $10^7$  m s<sup>-2</sup>, thereby demonstrating its potential to be exploited for integrated on-chip mixing, concentration, and separation.

For these inertial flows, the migration of any particles suspended in the flow across the primary flow streamlines into the vortex is governed by a sudden loss of the wall lift  $F_w$  when the particles enter the chamber. As a consequence, there no longer exists an opposing force arising from hydrodynamic interactions of the particle with the wall, which, when present as the particle was moving through the microchannel, had countered the shear gradient lift on the particle  $F_s$  that causes it to migrate down the shear gradient away from the channel centerline to a new equilibrium position in the channel. Once devoid of this balancing force, the particles are able to escape the primary flow to enter into the vortex under the slowly decaying shear gradient lift force, which scales with the particle size as  $C_L d_p^4$  if  $d_p/W \ll 1$ ,<sup>[150]</sup> where  $C_L$  is the lift coefficient and  $W$  the channel width, which in itself scales as  $1/d_p^2$  (see, for example, **Figure 1b**).<sup>[151]</sup> Larger particles, experience high shear gradient lift, and therefore migrate faster into the vortex in addition to their tendency to

**Table 1.** Mechanisms employed to generate centrifugal flows in microfluidic devices.

		Limitations	
		Advantages	
		Passive actuation mechanisms	
Geometry	<p>Cavity/Chamber</p> <ul style="list-style-type: none"> <li>• Single chamber<sup>[19–21]</sup> <ul style="list-style-type: none"> <li>– Multiple inlet/outlet<sup>[22–24]</sup></li> </ul> </li> <li>• Dual/multiple chambers<sup>[25–31]</sup></li> <li>• Viscoelastic instabilities<sup>[32–36]</sup></li> </ul> <p>Converging/corner flows<sup>[37–39]</sup></p> <p>Dean flows</p> <ul style="list-style-type: none"> <li>• Bend<sup>[40]</sup></li> <li>• Serpentine<sup>[41–44]</sup></li> <li>• Spiral<sup>[45–47]</sup></li> <li>• Alternating symmetry (e.g., zigzag)<sup>[48]</sup></li> </ul>	<p>Simple, effective, and potentially low-cost</p>	<p>Considerable pressure drop necessitates large benchtop pumps to drive the flow</p> <p>Not possible to tune centrifugation intensity independent of flow for a given device</p> <p>Dead volumes around corners in cavities, chambers, and sharp bends/turns can lead to particle deposition and fouling</p> <p>For viscoelastic instabilities to be exploited, the working solution needs to be natively elastic or additives need to be included to endow it with elastic properties</p>
Topology	<p>Microfabricated structures</p> <ul style="list-style-type: none"> <li>• Wall protrusions<sup>[49]</sup></li> <li>• Grooves<sup>[160,161]</sup></li> <li>• Posts <ul style="list-style-type: none"> <li>– Flow deformation<sup>[50]</sup></li> <li>– Vortex shedding<sup>[51,52]</sup></li> </ul> </li> </ul> <p>Combined with geometrical features<sup>[53–55]</sup></p>	<p>Simple, effective, and potentially low-cost</p>	<p>Considerable pressure drop necessitates large benchtop pumps to drive the flow</p> <p>Not possible to tune centrifugation intensity independent of flow for a given device</p> <p>Dead volumes around corners in cavities, chambers, and sharp bends/turns can lead to particle deposition and fouling</p>
Electrokinetic actuation	<p>Linear DC electrokinetics: nonuniform <math>\zeta</math>-potential<sup>[56]</sup></p> <ul style="list-style-type: none"> <li>• Polymer coatings<sup>[57]</sup></li> <li>• pH gradients via electrolytic reactions<sup>[58]</sup></li> </ul> <p>Nonlinear DC electrokinetics</p> <ul style="list-style-type: none"> <li>• Singular fields at sharp insulated corners<sup>[59,60]</sup></li> <li>• Ion exchange granules/membranes<sup>[45,61–65]</sup></li> <li>• Ideally polarizable surfaces<sup>[66]</sup></li> </ul> <p>Nonlinear AC electrokinetics</p> <ul style="list-style-type: none"> <li>• AC electroosmotic flow <ul style="list-style-type: none"> <li>– Capacitive charging<sup>[67–70]</sup></li> <li>– Faradaic charging<sup>[68,71,72]</sup></li> </ul> </li> </ul> <p>Electrothermal effect<sup>[73–82]</sup></p> <p>Interfacial electrokinetics</p> <ul style="list-style-type: none"> <li>• Discharge-driven<sup>[83–87]</sup></li> <li>• Electrowetting<sup>[88]</sup></li> </ul>	<p>Ease of electrode fabrication and integration into microfluidic device if large applied potentials requiring bulky amplifiers are not required</p> <p>Electric field intensity can be tuned to control vortex characteristics and strength</p>	<p>Chemical surface modification is an added complexity in channel fabrication; functionalization can wear off and needs to be reapplied</p> <p>Large DC currents, particularly singular fields at sharp corners, can generate not only Joule heating but also bubbles and ionic contamination which can lead to channel clogging, or, molecular denaturation and cell lysis</p> <p>Use of ion exchange granules is intrusive; ion exchange membranes are susceptible to fouling and can lead to large pressure drops which necessitate large pumping effort</p> <p>Optical setup to generate electrothermal flow may not be miniaturizable and hence easily integrated</p> <p>Evaporation effects where interfaces are present</p> <p>Large kV potentials required to generate corona discharge; fabrication of sharp electrode in air is impractical</p>

**Table 1.** Continued.

	Advantages	Limitations
	Active actuation mechanisms	
<b>Acoustic actuation</b>	<p><b>Bulk vibration</b></p> <ul style="list-style-type: none"> <li>• Indirect, i.e., oscillating surfaces</li> <li>– Bubbles<sup>[89–99]</sup></li> <li>– Posts/pillars/protrusions/ chamber<sup>[100–105]</sup></li> <li>– Membranes<sup>[106]</sup></li> <li>– Resonant cavities<sup>[107,108]</sup></li> <li>– Microarray titer plate<sup>[109]</sup></li> <li>– Plasmonic nanoparticles (photoacoustic effect)<sup>[110,111]</sup></li> <li>• Direct contact with liquid<sup>[112–117]</sup></li> </ul> <p><b>Surface vibration</b></p> <ul style="list-style-type: none"> <li>• Sessile droplet: azimuthal flow via symmetry breaking<sup>[118–126]</sup></li> <li>• Microchannel <ul style="list-style-type: none"> <li>– Standing waves: local recirculation<sup>[127]</sup></li> <li>– Travelling waves; longitudinal<sup>[128]</sup></li> <li>– Travelling waves; transverse<sup>[128]</sup></li> <li>– Vortex beam<sup>[129–131]</sup></li> </ul> </li> <li>• Indirect coupling <ul style="list-style-type: none"> <li>– Superstrate<sup>[132,133]</sup></li> <li>– Phononic crystal<sup>[134,135]</sup></li> <li>– Capillary tube<sup>[136]</sup></li> <li>– Lab-on-a-disc<sup>[137,138]</sup></li> </ul> </li> </ul> <p>Hybrid bulk and vibration (coupling into microarray titer plate)<sup>[139,140]</sup></p>	<p>Bubbles are relatively difficult to stabilize and thus have limited lifetimes</p> <p>Plasmonic nanoparticles can contaminate sample and can be difficult to remove</p> <p>Low (Hz/kHz) frequency operation typically associated with bulk waves are relatively inefficient particularly due to viscous heating, and can often inflict cavitation, shear, and thermal damage on biomolecules and cells</p> <p>Bulk vibration usually driven using large transducers, which are not easily miniaturized and integrated</p> <p>Piezoelectric substrates are generally more expensive than the typical materials used to fabricate microfluidic devices (e.g., soft polymers or silica)</p>
<b>Thermal actuation</b>	<p><b>Bulk convection</b></p> <ul style="list-style-type: none"> <li>• Density gradients (Rayleigh–Bénard)<sup>[141,142]</sup></li> <li>• Substrate energy gradients<sup>[141,142]</sup></li> </ul> <p><b>Surface shear</b></p> <ul style="list-style-type: none"> <li>• Thermocapillary effect<sup>[143]</sup></li> <li>• Evaporation<sup>[144,145]</sup></li> </ul>	<p>Difficult to incorporate local heating elements</p> <p>Precise thermal control can be difficult to achieve</p> <p>System is not easily reconfigurable to tune centrifugation intensity once heating elements are integrated</p> <p>Heating is one-off and irreversible (i.e., cannot reverse heating effects easily and need to constantly add additional heat to continually drive the actuation)</p> <p>Heat can lead to molecular and cell damage</p>
<b>Mechanical &amp; pneumatic systems</b>	<p><b>Microimpellers</b></p> <ul style="list-style-type: none"> <li>• Electrical actuation<sup>[146]</sup></li> <li>• Vibrational actuation</li> <li>• Direct (SAW substrate contact)<sup>[147]</sup></li> <li>• Indirect (SAW microcentrifugal flow)<sup>[148]</sup></li> </ul> <p>Pneumatically driven air shear<sup>[149]</sup></p>	<p>Mechanically moving parts are susceptible to wear and reliability issues</p> <p>Pneumatic systems, giving their size, are not easily miniaturizable and integrated</p>



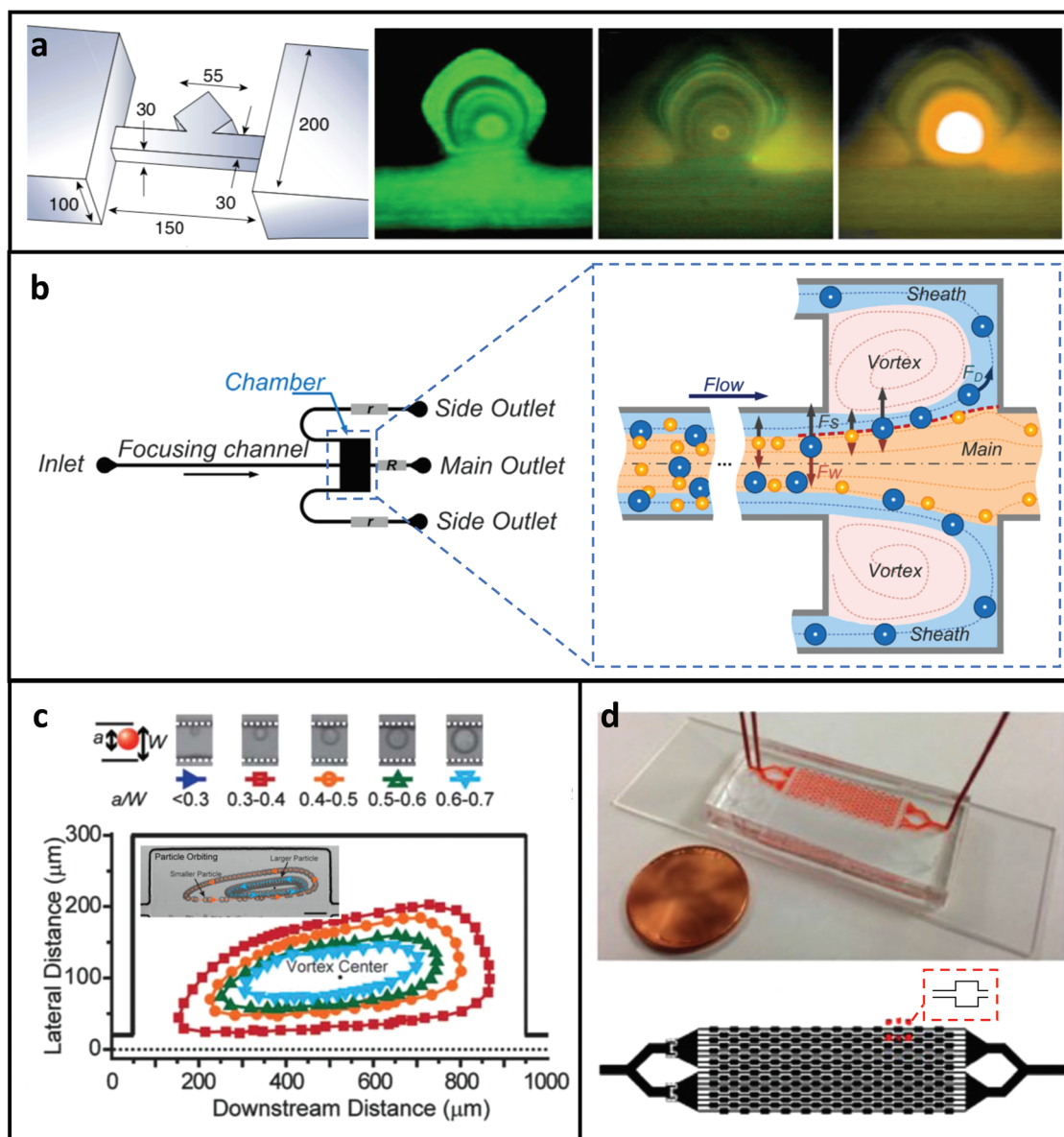


**Figure 1.** Vortex generation via microfluidic cavities. a) Schematic design (left panel) of a side cavity offshoot to a microchannel, in which a vortex is generated (right panels) and demonstrated for particle concentration and separation based on their densities (Reproduced with permission.<sup>[19]</sup> Copyright 2003, Nature Publishing Group; Reproduced with permission.<sup>[20]</sup> Copyright 2006, Springer-Verlag). b) Dual cavity with accompanying side channel outlets for particle recovery; also shown is a schematic showing the mechanism for particle separation due to inertial lift (Reproduced with permission.<sup>[27]</sup> Copyright 2013, AIP Publishing LLC). c) Particle size  $a$  dependent orbital trajectory within the vortex generated in a side cavity;  $W$  is the channel width (Reproduced with permission.<sup>[25]</sup> Copyright 2011, The Royal Society of Chemistry). d) Multiple cavity array (Adapted under the terms of a Creative Commons Attribution 4.0 license.<sup>[28]</sup> Copyright 2017, The Authors, published by Springer Nature and Hormel Institute).

populate orbits closer to the center<sup>[25]</sup> (Figure 1c), which can be determined from a dominant balance between the centrifugal and viscous forces acting on the particle<sup>[22,23]</sup>

$$\frac{r_{p,0}}{r_{p,t}} = \exp \left[ \frac{d_p^2 (\rho_p - \rho) \omega^2 t}{18\eta} \right] \quad (1)$$

In the above,  $r_{p,0}$  and  $r_{p,t}$  are the orbital radius of the particle from the vortex center  $r_p$ , initially at time  $t = 0$  and subsequently

at time  $t$ , respectively,  $\rho$  is the liquid density, and  $\omega$  the flow angular velocity.

If this shear gradient lift force is balanced by the drag force on the particle  $F_D \approx 3\pi\eta\nu_p d_p$ , then the tangential particle velocity  $v_p$  scales linearly with  $d_p$  suggesting larger particles migrate faster across the streamlines. This particle size discrepant scaling (although we note that the complexity of other factors that affect the flow and particle dynamics leads to a range of different scalings—see, for example, ref. [25]) was taken advantage to isolate large circulating tumour cells that migrate over

shorter distances and hence enter into the vortex while leaving the smaller red and white blood cells in the primary flow;<sup>[30]</sup> in ref. [27], two side outlets as siphoning channels were included to the chamber (Figure 1b) to create a sheath flow that facilitated the removal of the particles that were entrained in the vortex. Once inside, the particles only remain within the vortex if the effective centrifugal force acting on the particle is insufficient to balance the shear gradient lift. As the centrifugation force is dependent on the particle density, i.e.

$$F_c = \frac{(\rho_p - \rho) \pi d_p^3 v_p^2}{6r_p} \quad (2)$$

particles can be sorted by their density since heavier particles would tend to leave the vortex once having entered it. Such an ability to discriminate particles based on their sizes or densities, together with a variety of other uses such as single cell rotation, molecular trapping, and even the analysis of microorganism motility, among other applications, have been demonstrated using this platform.<sup>[20,152,153]</sup> Triggering the release of all particles from the vortex, however, would necessitate the suppression or complete annihilation of the vortical flow by altering the inlet conditions, for example, by decreasing the inlet flow rate.

Other variants to the single microchannel cavity design have also been explored, including the introduction of bidirectional flow through top and bottom channels flanking the rectangular or circular cavity to enhance the rotational flow intensity,<sup>[22,23]</sup> and the incorporation of an inlet channel above the chamber as a source to generate rotational flow within it,<sup>[23]</sup> or an outlet at the top of the cavity for separating out the concentrated particles.<sup>[24]</sup> The inline expansion chamber design shown in Figure 1b<sup>[25–28]</sup> can be considered a dual-cavity variant to the single cavity design although we note that in this case, the entire channel flow expands into the chamber to generate a pair of vortices; the vortex pair is expected to remain symmetric as long as the flow does not become unstable beyond a critical Reynolds number,<sup>[154]</sup> breaking the symmetry of the microchambers and hence the vortices that are generated within, on the other hand, was shown to be useful, for example, in facilitating control over the chirality in the assembly process of supramolecular systems.<sup>[155]</sup> Extensions in the microchamber designs to increase the throughput and efficiency of separation, for example, for sequential cell enrichment or tumour cell isolation, was also demonstrated through multiplexing wherein a large number of inline chambers arrays, both in series and in parallel were employed<sup>[25,29–31]</sup> (Figure 1d).

Converging (e.g., hydrodynamic focusing),<sup>[37]</sup> as well as corner flows (e.g., flow over a notch<sup>[38]</sup>) or flows over sharp bends, have also been explored for vortex generation in microchannels. In addition, we note an interesting design involving a corner cavity flow that was reported by Tsai et al.<sup>[39]</sup> in which a series of adjacent vortical flows in alternating directions, thus mimicking a series of mechanical gears, are generated (Figure 2). The number of vortices and their size depends on the pressure at which the flow is driven at, although we note that fairly large pressures are required due to the considerable pressure losses that occur in the channel.

Taking a leaf from macroscopic Dean flows—secondary flows that occur in a transverse direction to the main channel axis which are a consequence of the radial pressure gradient

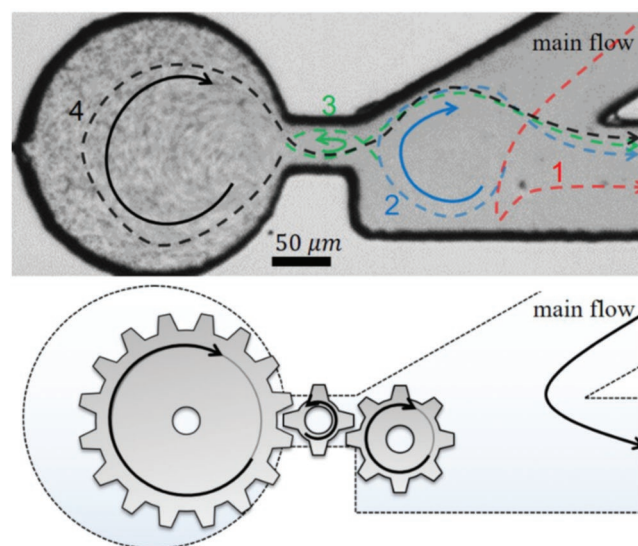


**Figure 2.** Virtual vortex gear: vortical formation in an offshoot channel (top) design that resembles a mechanical gear system (bottom) (Reproduced with permission.<sup>[39]</sup> Copyright 2018 AIP, Publishing LLC).

generated due to centrifugal effects arising from the channel's curvature—helices or twists in the channel geometry, curvilinear designs such as the serpentine, spiral, and zigzag arrangements,<sup>[40–48]</sup> some of which are shown in Figure 3, have also been integrated into microfluidic channels to induce some degree of rotation in the flow. The intensity of the Dean flow and hence the vorticity that is generated largely depends on a balance between the inertial stresses that drive the primary axial flow and the centrifugal force, and can be characterized by a Dean number  $Dn \equiv (D_H/R)^{1/2} Re$ , wherein  $D_H \equiv 4A_c/P$  is the hydraulic diameter of the channel, with  $A_c$  being the cross-sectional area and  $P$  the wetted perimeter,  $R$  the radius of curvature of the flow path, and  $Re$  the Reynolds number with a characteristic lengthscale is defined by  $D_H$ .<sup>[156,157]</sup>

As with all other passive actuation methods, an inevitable downside of exploiting geometrical features to generate vortices in the flow, beyond the lack of an active flow control mechanism, is the large pressure drop encountered due to the additional channel length required to accommodate its tortuosity, and hence the necessity for large pumps to drive the flow. This is compounded by the need for an adequate pressure head, as can be seen from the dependence of  $Dn$  on  $Re$  above, in order to drive adequate transverse flow to move the fluid radially from the inner to outer channel walls so as to generate a sufficient centrifugal force to disrupt the laminar primary axial flow; as such, Dean numbers in microfluidic devices typically do not exceed 100,<sup>[40]</sup> especially without resorting to the extreme curvatures ( $d/R \gg 1$ ) that exacerbate pressure losses in the channel or the high flow rates that lead to high sample or reagent utilization.

An alternative for driving secondary flows in microchannels but without requiring inertial dominance in the system is to exploit viscoelastic instabilities. However, unless the working solution possesses some native elasticity, such as DNA solutions or some micellar solutions in the presence of specific additives, this requires the working solution to be spiked with

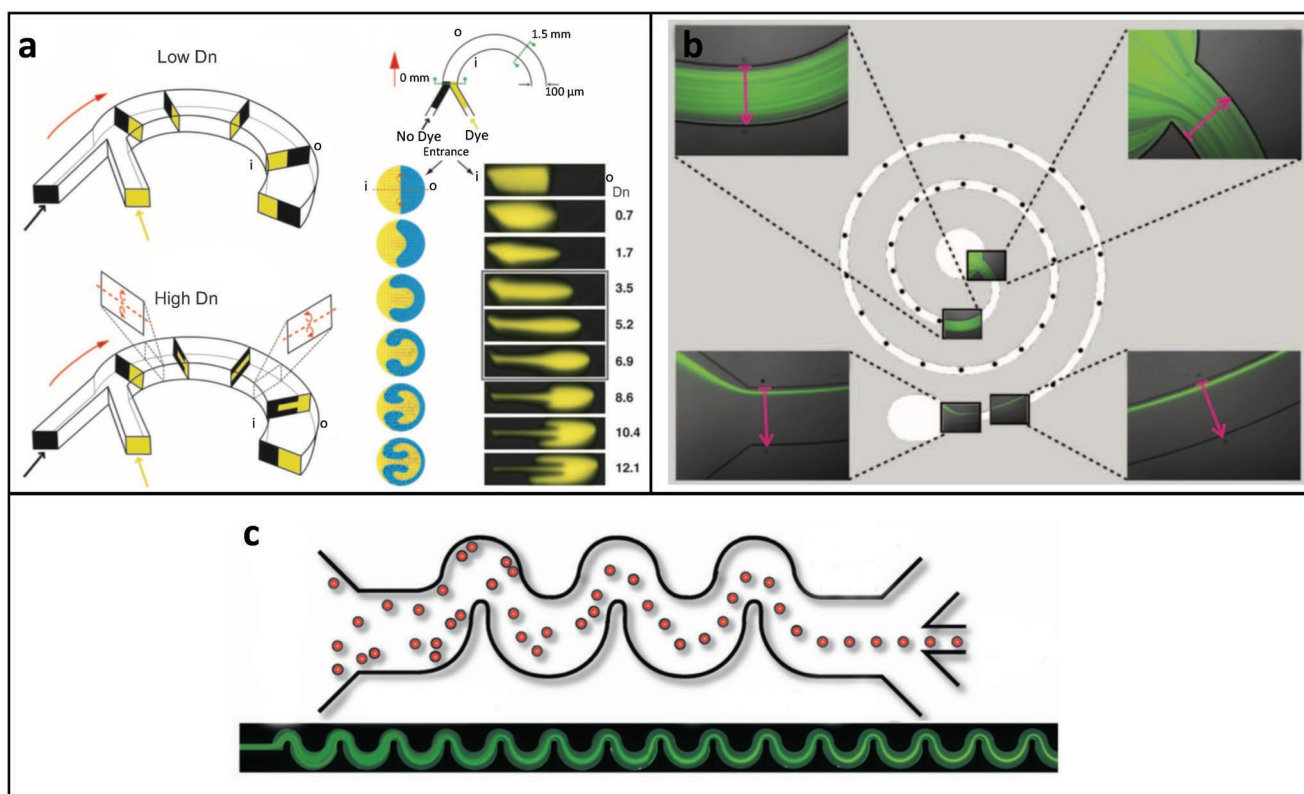


**Figure 3.** Vortex generation via microfluidic geometries. a) Curved channel arrangement at low ( $Dn \approx 1$ ) and high ( $Dn \approx 10$ ) Dean numbers (Reproduced with permission.<sup>[40]</sup> Copyright 2006, The National Academy of Sciences of the USA). b) Spiral channel arrangement (Reproduced with permission.<sup>[47]</sup> Copyright 2012, AIP Publishing LLC). c) Serpentine channel arrangement (Reproduced with permission.<sup>[44]</sup> Copyright 2007, The National Academy of Sciences of the USA).

small amounts of polymers, which may not always be practical nor expedient. The instabilities, which occur above a critical condition<sup>[158]</sup>

$$M_{\text{crit}} \leq \left( \frac{\lambda U}{R} \frac{\tau}{\eta_0 \dot{\gamma}} \right)^{1/2} \quad (3)$$

wherein  $\lambda$  is the polymer relaxation time,  $R$  the radius of curvature,  $\tau$  the normal stress in the flow direction,  $\eta_0$  the zero-shear-rate viscosity, and  $\dot{\gamma}$  the shear rate, are a consequence of the low Reynolds number coupling between the elastic stretching of the long, flexible polymeric chains in the solution when the flow is subjected to curvature effects<sup>[159]</sup> in the various microfluidic geometries discussed above such as the contraction and expansion slots that produce the converging or diverging flows, or the serpentine channels, as well as that due to flows over sharp bends.<sup>[32–36]</sup> The upstream corner vortices that arise—a viscoelastic version of the Moffatt vortices in Newtonian creeping flows, as illustrated in **Figure 4a,b**—are dependent on the nature and the aspect ratio of the geometry, as well as the rheological properties of the fluid, and are thus influenced by the Elasticity number  $El \equiv Wi/Re$ , wherein  $Wi \equiv \lambda \dot{\gamma}$  is the Wiessenberg number which captures the relative contributions between the elastic and viscous stresses in the flow and  $Re \equiv \rho U D_H / \eta \dot{\gamma}$ , and could eventually become 3D and unstable.<sup>[34]</sup> A phase map showing the transition to instability

for nonshear-thinning viscoelastic polyethylene oxide solutions is shown in **Figure 4c**.<sup>[33]</sup>

## 2.2. Topology

In the opposite case to a cavity, vortices can also be generated passively around protrusions to the flow along the channel walls (**Figure 5**).<sup>[49]</sup> More generally, the incorporation of a variety of repeating topological features into the microfluidic channel has been explored to induce flow recirculation. An early example of introducing such topology into the channel is the staggered herringbone structure in ref. [160], which facilitated the generation of transverse recirculation cells in the plane orthogonal to the axial flow along the microchannel (**Figure 6a**). This was demonstrated to enhance passive micromixing along the channel—a concept later employed to increase cell binding to antibody moieties on the channel surface so as to enhance isolation of circulating tumor cells.<sup>[161]</sup>

Another example of the use of topological features to generate recirculatory flows is through the introduction of micro-fabricated post arrays in a microfluidic device. The obstruction that these posts impose to a flow with sufficient inertia either causes it to deform,<sup>[50]</sup> or acts as a bluff body behind which fluctuations in the hydrodynamic pressure gives rise to periodic vortex shedding beyond a critical Reynolds



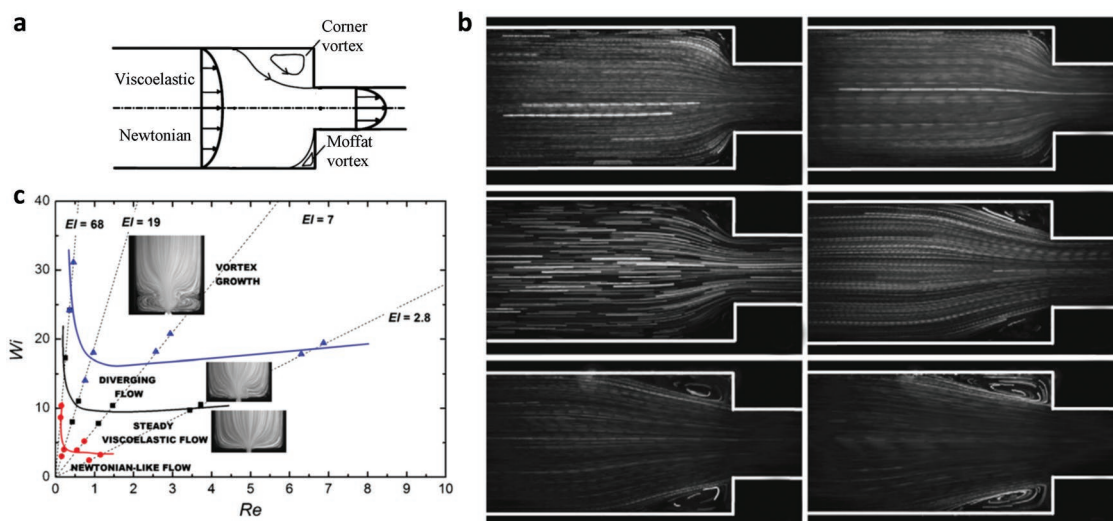


**Figure 4.** Vortex generation in viscoelastic flows. a,b) Corner vortices (top half of channel) arising behind microchannel constrictions in viscoelastic flows, which are similar to Moffat vortices in Newtonian creeping flows (bottom half of channel) (Reproduced with permission.<sup>[34]</sup> Copyright 2008, Elsevier B.V.). c) Phase map in  $Wi-Re$  space delineating the transition toward viscoelastic instability in nonshear-thinning viscoelastic polyethylene oxide solutions (Reproduced with permission.<sup>[33]</sup> Copyright 2008, Elsevier B.V.).

number.<sup>[51,52]</sup> In the former, the inertia in the system breaks the fore-aft symmetry of the flow around a post that is typically expected in viscous systems (i.e., Stokes flows) such that there is sufficient fluid deformation in the flow, which, when under confinement by the channel boundaries, gives rise to net recirculation; Amini et al. showed that it is possible to tune both the position as well as the structure of the recirculation by judicious choice in the lateral placement of successive pillars in the channel (Figure 6b).<sup>[50]</sup> Further increases in the Reynolds number beyond a critical value, however, leads to boundary layer separation from the post surface, and hence vortex shedding (Figure 6c). Such vortex shedding, whose frequency  $f$ —as characterized by a Strouhal number  $Sr \equiv fL/U$ , in which  $L$  is the characteristic length scale of the posts and  $U$  the mean velocity of the flow between them—increases with a decrease in the feature aspect ratio and increasing longitudinal confinement of the flow between the posts, i.e., smaller pitch-to-post diameter ratios,<sup>[51]</sup> and was shown to be effective not only to sufficiently permeabilize cell membranes in order to deliver an exogenous payload comprising various therapeutic molecules into the cell to aid transfection, but to also lyse the cells.<sup>[52]</sup> Additionally, topology has also been combined with geometrical features to enhance vorticity generation in microchannels.<sup>[53–55]</sup>

### 3. Active Actuation

As with driving microfluidic actuation in general, be it sessile droplet transport and manipulation (e.g., splitting and recombination), flow dispensing and microchannel pumping, a number of options in terms of external forcing mechanisms are available that can be harnessed for generating flow recirculation in microfluidic devices, each with their own advantages and disadvantages.

#### 3.1. Electrokinetics

Electric fields are simple to generate given the ease of electrode fabrication and integration within the microfluidic device. In the absence of internal pressure gradients, flows driven by direct current (DC) electroosmosis at small scales commensurate with microfluidic devices, quite unexpectedly, however, constitute potential flows given the coincidence between the hydrodynamic streamlines with the electric field lines, which are solenoidal in nature (i.e., the electric field has to satisfy the divergence-free condition), and, by virtue of irrotational.<sup>[162]</sup> It is nevertheless possible to revoke the potential flow and electric field similarity, for example, by introducing nonuniformity in the  $\zeta$ -potential (the potential drop across the Debye double layer), and consequently the electrokinetic slip velocity

$$u_s = -\frac{\varepsilon\zeta(x)}{\eta} \left[ E_t + \frac{1}{4} \frac{d\zeta(x)}{dx} \right] \quad (4)$$

wherein  $\varepsilon$  is the electric permittivity and  $E_t$  the applied tangential ( $x$ -axis) electric field—along the microchannel,<sup>[56]</sup> either by varying the surface chemistry,<sup>[57]</sup> for instance through the use of polymer coatings to create patterns in the surface charge<sup>[163]</sup> or through the introduction of pH gradients via electrolytic redox reactions that drive ion adsorption on the channel surface,<sup>[58]</sup> although the practicalities associated with such endeavors may be questionable.

To circumvent this, it is possible to exploit a branch of electrokinetics wherein the polarization of the double layer, which constitutes the primary source of ions responsible for driving electrokinetic actuation, is induced by an external electric field instead of the surface charges, and hence is independent of the surface chemistry. Such field-induced polarization, known as induced-charged electrokinetic phenomena,<sup>[164]</sup> is inherently nonlinear since the  $\zeta$ -potential is now also a function of

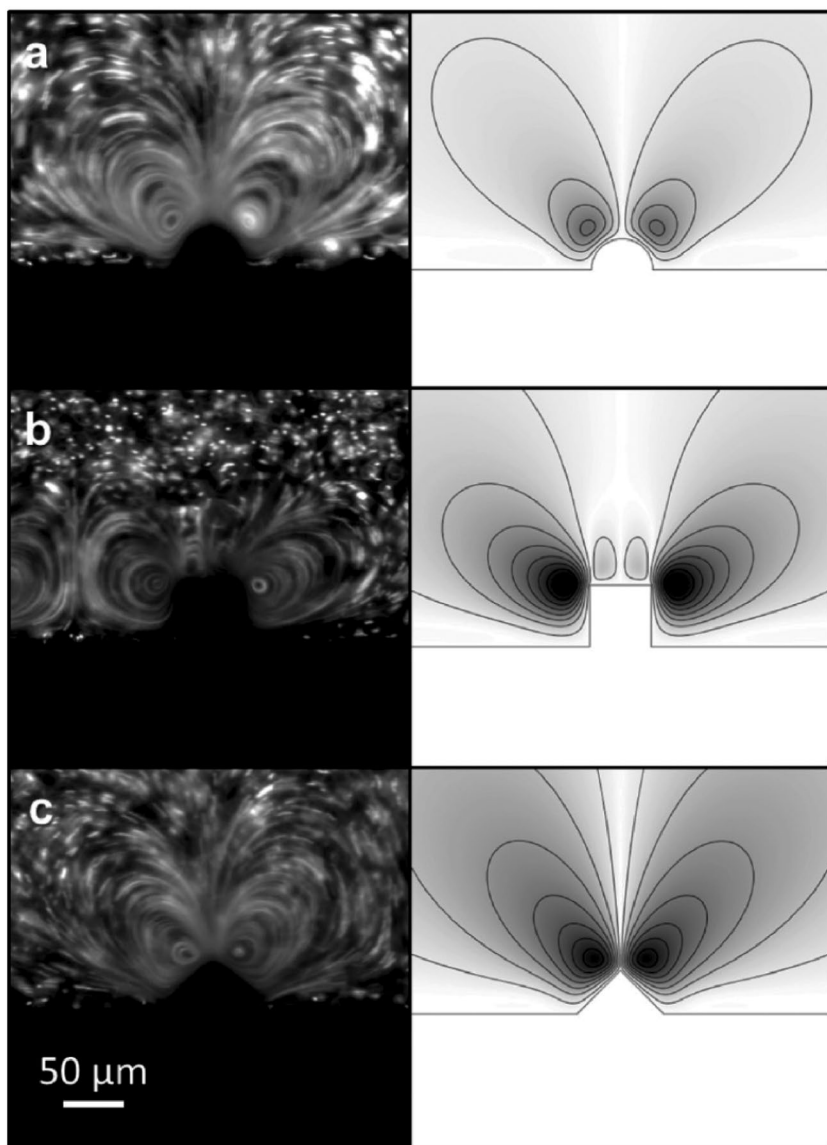


**Figure 5.** Vortex generation around protrusions in a microchannel wall comprising a variety of shapes: a) circle, b) square, and c) triangle; the left column shows the experimental images and the right column shows the corresponding computational flow streamlines (Reproduced with permission.<sup>[49]</sup> Copyright 2012, American Chemical Society).

the electric field, i.e., and results in a departure from equilibrium.<sup>[162]</sup> For a DC electric field, this can arise if there is sufficient normal electric field to overcome the screening effect of the counter-ions in the double layer such that surface penetration leading to induced space charging occurs. One way to achieve this is through the generation of large singular electric fields at sharp insulated corners, which facilitate field penetration across the double layers along the corner,<sup>[59,60]</sup> which, in turn leads to a converging stagnating nonlinear electroosmotic flow that manifests as a jet and recirculating flow at the corner<sup>[68]</sup> (Figure 7a).

Another way is to employ a porous ion-exchange granule that, due to its ion specificity, permits counter-ions to enter one-half of the granule, therefore giving rise to an electromigration

flux that allows the normal field to penetrate the double layer,<sup>[166]</sup> resulting in broken flow-field similarity since the streamlines themselves do not enter the granule. A co-ion depletion region also exists given the requirement for electroneutrality at the granule surface where the counter-ions enter the granule and the potential drop across this region, which is a function of the normal field  $E_n$ , replaces the  $\zeta$ -potential in the expression for the slip velocity, such that it is now nonlinear. Since  $E_n$  varies from a minimum at the pole of the granule ( $\theta = 0$ ) to a maximum at the equator ( $\theta = \pi/2$ ) due to its curvature, the slip velocity, which can be shown to scale as  $\sin \theta \cos \theta$  increases to a maximum at  $\theta = \pi/4$ .<sup>[167]</sup> As a consequence of the back pressure buildup at the equator, a recirculating vortex therefore arises at this location due to flow continuity (Figure 7b), which has been exploited for micromixing and analyte preconcentration.<sup>[45,61,62]</sup> In a manner not unlike the Rayleigh–Bénard instability in which a constant thermal flux introduces a vortex instability, it was shown that the constant ion flux in the extended polarization layer away from the porous surface can drive a vortex instability whose length scale coincides with the size of the extended polarization zone, which, in turn, scales as the thickness of the electroneutral diffusion layer that separates it from the bulk Ohmic region (Figure 7c).<sup>[63–65,168]</sup>

In a manner akin to the recirculation flow generated around the ion-exchange granule via DC field-induced polarization in Figure 7b, it is also possible to generate similar streaming flows, albeit at considerably lower potentials, on ideally polarizable surfaces (besides the electrode surface) such as conducting cylinders or spheres, which are able to attract the field lines so that they penetrate, predominantly in the orthogonal direction, into the double layer. Squires and Bazant<sup>[66]</sup> showed that the time-averaged

electroosmotic slip along the azimuthal surface  $\theta$  of a cylinder of diameter  $a$  under an external field  $E = E_\infty \exp(i\omega t)$ , with  $i \equiv (-1)^{1/2}$ ,  $\omega = 2\pi f$  being the angular frequency and  $t$  the time, reads

$$\langle u_s(\theta) \rangle = \frac{\epsilon E_\infty^2 a}{\eta} \frac{\sin \theta}{1 + \omega^2 \tau_c^2} \quad (5)$$

Here,  $\tau_c \sim \lambda_D a / D$  is the characteristic double layer charging time in which  $D$  is the diffusivity. It was then shown that this slip is accompanied by a pair of recirculating vortices when the net charge of the cylinder  $Q > 0$  (Figure 8).

To circumvent the disadvantages associated with DC electrokinetics, namely, the large DC currents that can not only result in molecular denaturation and cell lysis, particularly in the

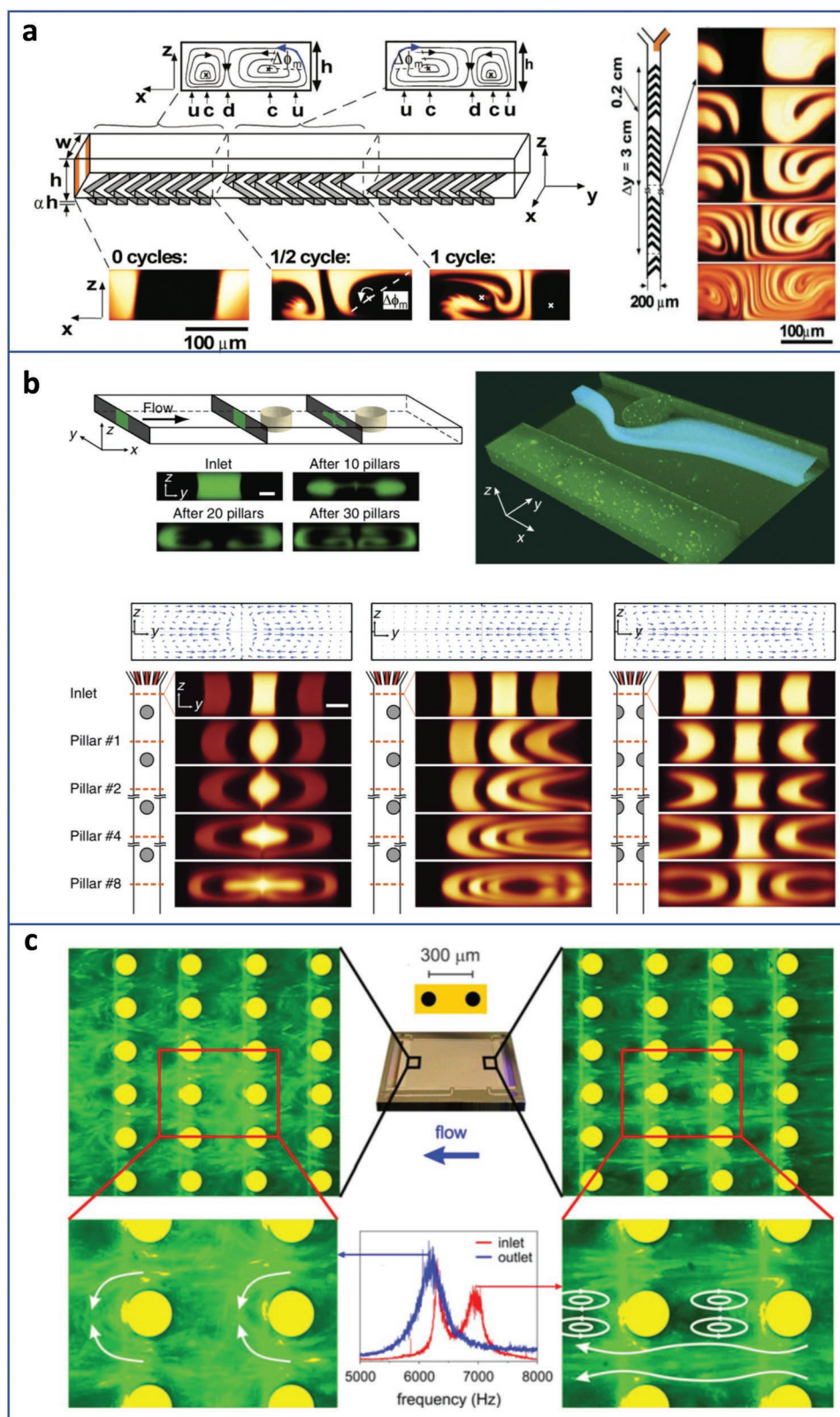


**Figure 6.** Vortex generation through the incorporation of microchannel topological features. a) Staggered herringbone patterns; “c,” “u,” and “d” denote the centers of rotation, and the upwelling and downwelling of the vortices that are generated, respectively (Reproduced with permission.<sup>[160]</sup> Copyright 2002, American Association for the Advancement of Science). b) Pillar arrays (Reproduced with permission.<sup>[50]</sup> Copyright 2013, Macmillan Publishers Ltd.). c) Vortex shedding behind pillar arrays; the left shows the case for moderate frequencies and hence moderate Strouhal numbers  $S_r$ , whereas the right shows the case for high frequencies and hence large  $S_r$  (Reproduced with permission.<sup>[51]</sup> Copyright 2013, Springer-Verlag).



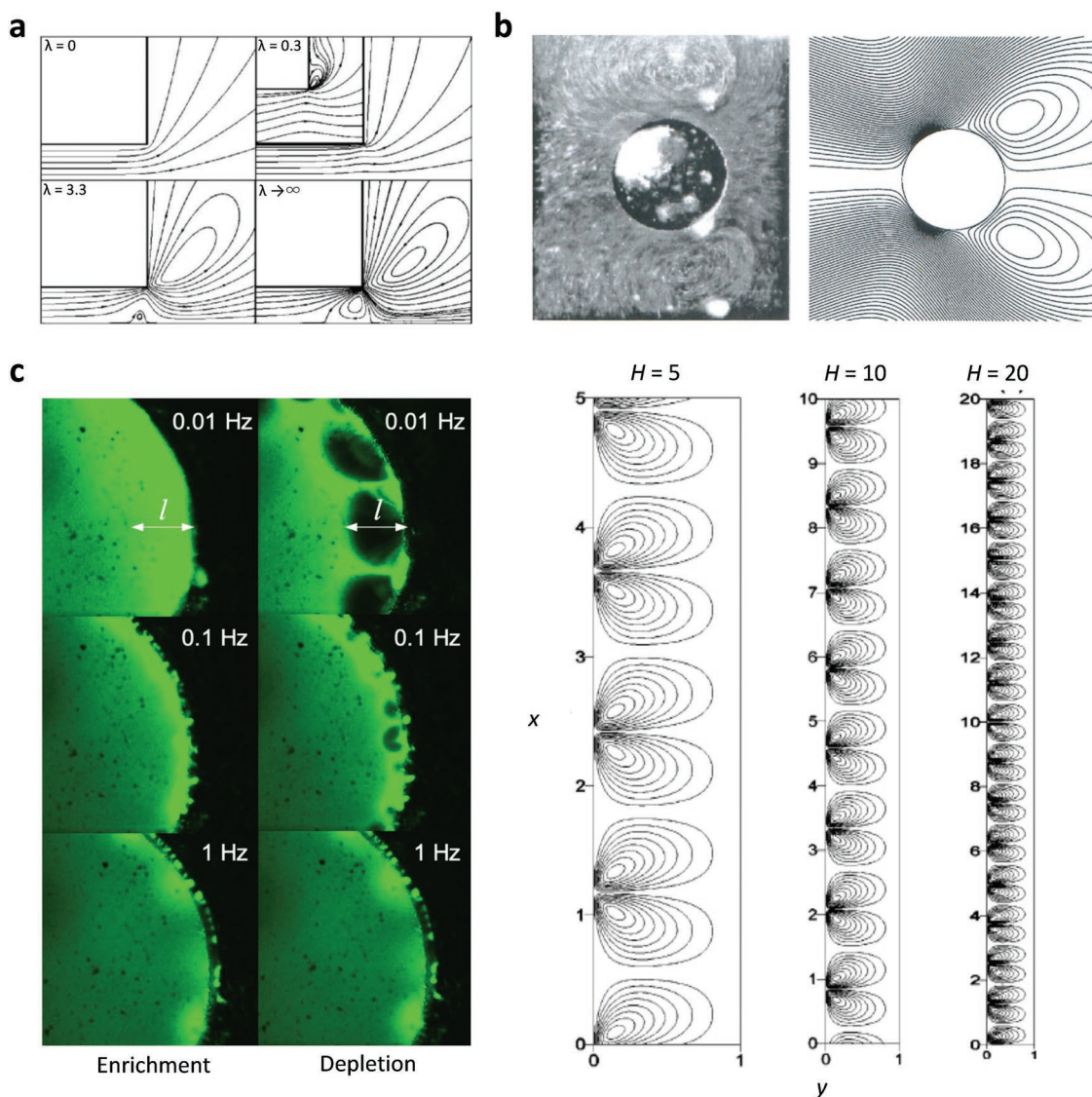


**Figure 7.** DC electrokinetic vortices. a) Recirculation generated by singular electric fields at sharp insulated corners; the parameter  $\lambda$  characterizes the relative contributions between the linear and induced components of the  $\zeta$ -potential, the latter due to field leakage through the corner (Reproduced with permission.<sup>[165]</sup> Copyright 2006, American Institute of Physics). b) Image (left) and numerical simulation (right) of vortex generation around a conducting ion selective granule (Reproduced with permission.<sup>[62]</sup> Copyright 2002, Cambridge University Press). c) Experimental image (left) showing the enrichment and depletion cycles for three different frequencies and numerical simulation (right) showing the vortex instability that arises along the extended polarization zone of a nanoporous membrane; the characteristic vortex length approximately scales with the thickness of the diffusion layer  $l$ , and is also dependent on the size of the finite element domain  $H$  given that the diffusion layer thickness is imposed in the numerical simulation (Reproduced with permission.<sup>[65]</sup> Copyright 2008, American Physical Society; Reproduced with permission.<sup>[63]</sup> Copyright 2002, American Physical Society).

presence of high conductivity buffers, but also cause significant Joule heating and Faradaic reactions which lead to the generation of bubbles and ionic contaminants, considerable attention has been paid to driving microfluidic actuation using high frequency (>10 kHz) electric fields.<sup>[162]</sup> At these frequencies, it is possible to invoke similar field-induced polarization to that discussed above, albeit in a much easier way by exploiting the transient effects associated with the AC field. A consequence of the dynamic nonequilibrium charging is the nonuniformity in the polarization along the electrode surface, which gives rise to back-pressure-driven vortices. An example of this can be observed in the AC electroosmotic flow that arises on the

symmetric co-planar electrodes illustrated in **Figure 9a** in which the normal charging of the double layer in every half AC cycle gives rise to a tangential field and hence Maxwell force. Despite the reversal of the applied field, this Maxwell force is always in the outward-facing direction as shown since the polarity of the charges that accumulate in the double layer also reverses, thus giving rise to a net nonzero time-average Maxwell stress and hence an oscillatory time-averaged electroosmotic slip with a velocity given by<sup>[67]</sup>

$$u_s = -\frac{\epsilon}{4\eta} \nabla_s \left[ \Phi \mp \frac{V_o}{2} \right]^2 \quad (6)$$

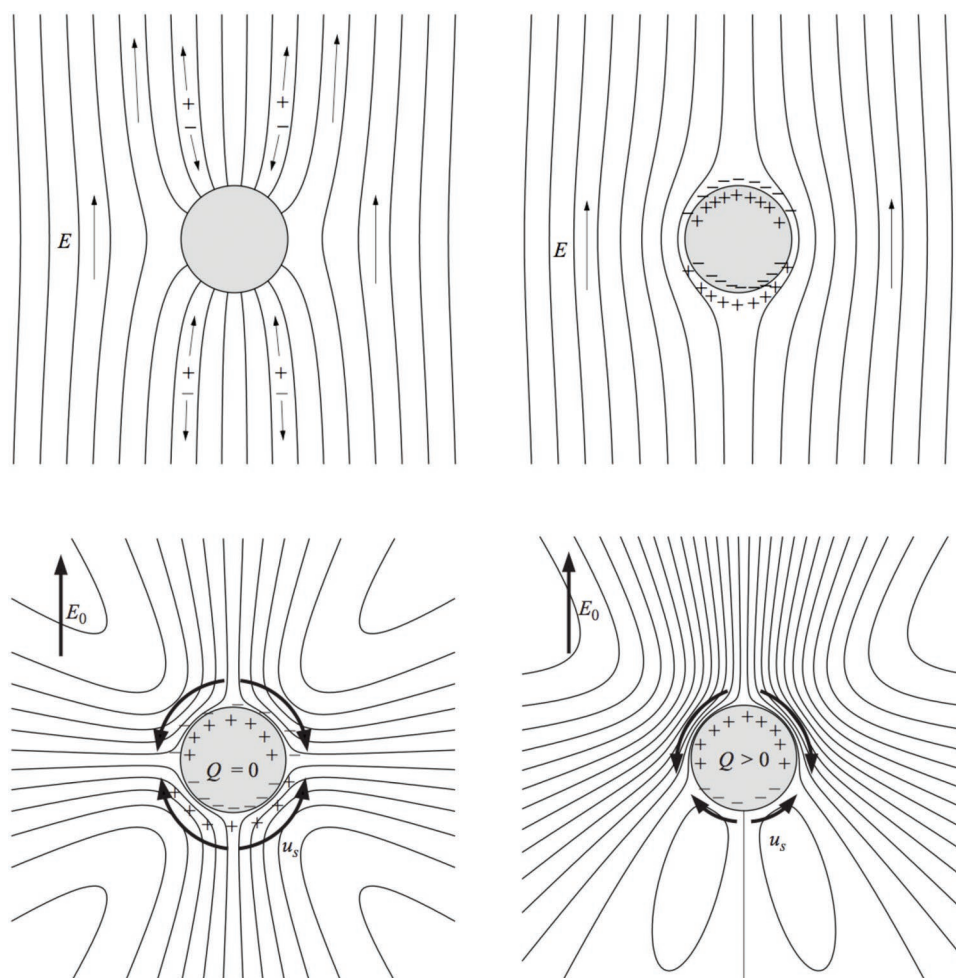


**Figure 8.** DC electrokinetic vortices. Electric field lines (top; the left image shows that for a partially charged double layer and the right shows that for a fully charged double layer) and streamlines (bottom; the left shows the case for zero net charge ( $Q = 0$ ) on the cylinder surface whereas that on the right shows the case where a net charge on the surface is present ( $Q > 0$ )) showing electroosmotic flow vortices arising due to double layer charging around a polarizable conducting cylinder immersed in an electrolyte (Reproduced with permission.<sup>[66]</sup> Copyright 2004, Cambridge University Press).

which due to the back pressure that is induced, produces a pair of recirculating vortices that are comparable to the electrode dimension, as shown. In the above,  $|V_0|$  is the RMS amplitude of the applied voltage,  $\Phi$  the potential in the bulk Ohmic region, and  $\nabla_s$  is the surface gradient operator acting across each electrode. A solution for  $\Phi$  is given by González et al.<sup>[67]</sup> such that the slip velocity can be determined.

In fact, for a symmetric co-planar electrode pair of width  $L$ , separated by a distance  $d$ , it was shown that along the electrode surface, two maxima with opposing polarity associated with the antisymmetric potential lines exist at  $L/2^{1/2}$  such that the electric field is zero and reverses directions at these points, as seen in **Figure 10a**. Since the electroosmotic slip velocity is proportional to the tangential field according to Equation (6), a stagnation point therefore exists at this location across which the slip velocity reverses direction. Flow continuity then results in a converging–stagnating flow around this point, giving rise to a vortex pair of dimension  $L/2^{1/2}$  and  $L(1 - 1/2^{1/2})$  over each electrode, which, together with the aid of a dielectrophoretic force, can be seen to lead to the trapping of particles along this electrode location

(**Figure 10b**). Such flows were shown to be useful, for example, for trapping bacteria<sup>[69]</sup> or for immobilizing and stretching individual DNA strands from a bulk solution<sup>[70]</sup> (**Figure 10c**).

If the applied voltage is increased such that the potential drop across the layer significantly exceeds  $RT/F$ , wherein  $R$  is the molar gas constant,  $T$  the absolute temperature, and  $F$  the Faraday constant, Faradaic reactions can give rise to ion generation or consumption at the electrodes such that the double layers are polarized through Faradaic charging in place of the capacitive charging mechanism described above. Since the ions generated in these reactions have the same polarity as that of the electrode, the double layers are oppositely charged to that due to capacitive charging and hence the flow direction is reversed to give rise to a diverging–stagnating flow instead, as illustrated in **Figure 9b**, thus presenting a means for dynamically erasing the particle assemblies in **Figure 10b,c** at will.<sup>[68,71,72]</sup> Alternatively, the converging–stagnating flow in **Figure 10b** can also be reversed by applying a DC bias wherein it was demonstrated that the induced dipole on particles suspended in the flow due to the applied AC field gives rise to a

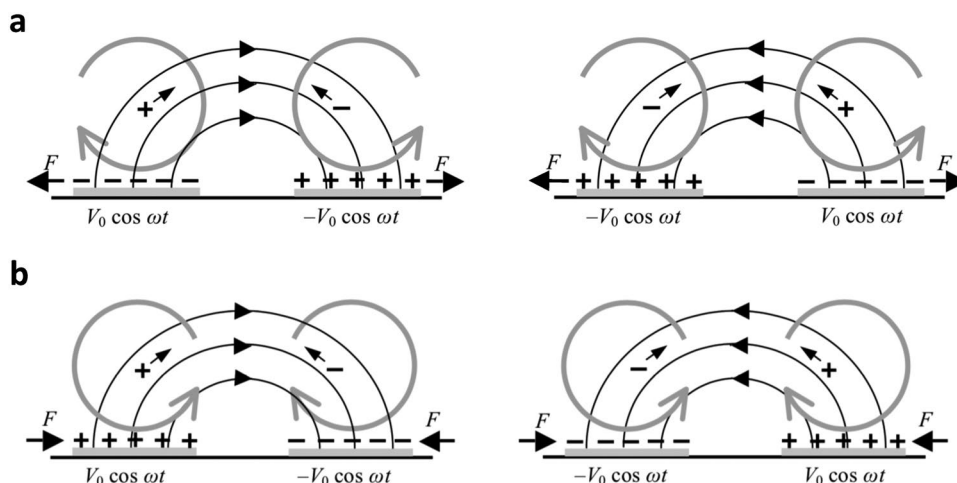


**Figure 9.** AC electrokinetic vortices. AC electroosmotic flow on symmetric co-planar electrodes due to a) capacitive and b) Faradaic charging, showing the direction of the electric field, the time-averaged force  $F$  that arises, and the corresponding flow profiles in successive AC half-cycles (Reproduced with permission.<sup>[162]</sup> Copyright 2010, Cambridge University Press).

uniform positive dielectrophoretic flux along the length of the electrodes that aggregates the particles into a cylindrical cloud-like structure that becomes unstable beyond a cluster dimension to break up into the concentric bands, which then merge into complex conical and butterfly-like structures, as seen in **Figure 11**.<sup>[169]</sup>

Finally, interfacial vortices can also be driven electrokinetically through a discharge-driven mechanism in which a singular electrode, held above the free surface and raised above a critical potential beyond which atmospheric breakdown occurs, leads to the generation of an ionic wind that can be exploited to shear the interface of a liquid in the form of a sessile droplet or in a microwell<sup>[83]</sup> (**Figure 12a**). This was then demonstrated for the trapping of particles within a vortex cluster due to shear induced migration along the surface<sup>[83]</sup> or a converging–stagnating flow in the bulk generated by the interfacial azimuthal rotation<sup>[84,85]</sup> for applications such as the separation of red blood cells from plasma<sup>[86]</sup> or for sample preconcentration to enable enhanced spectroscopic detection.<sup>[87]</sup> A theory that describes how the particles are trapped within the vortex center to a point or limit cycle, and strategies to break the vortex trap so as to release the particles, is given in Wang et al.<sup>[170]</sup> Additionally, it has also been shown that vortices can be generated within sessile droplets using electrowetting, wherein the application of the electric field leads to a change in the interfacial tension  $\gamma$  of the liquid and hence the contact angle  $\theta$  of the droplet<sup>[171,172]</sup>

$$\cos \theta = \cos \theta_0 + \frac{\epsilon V^2}{2d\gamma} \quad (7)$$

in which  $\theta_0$  is the native contact angle of the droplet prior to the application of the electric field,  $V$  is the applied potential and  $d$  the thickness of the dielectric layer separating the droplet from the plate electrode beneath it. As the application of the electric field only produces a static change in the contact angle as dictated by the Lippmann condition in Equation (7) above, it was necessary to drive the applied field from a low to high AC frequency (1–40 kHz) in order to excite capillary waves along the droplet interface, which, in turn, drives the internal flow

and hence the recirculating vortices within the droplet shown in **Figure 12b**.<sup>[88]</sup>

### 3.2. Acoustics

The flow arising along vibrating surfaces, typically in the form of circulation due to volume conservation, is known as acoustic streaming,<sup>[173–176]</sup> although the term has been loosely employed for all streaming phenomena, covering both acoustical phenomena wherein the flow arises due to dissipation of the sound wave energy as it propagates through a compressible fluid, as well as other phenomena that do not involve sound waves, such as that which arises in an incompressible fluid adjacent to an oscillating body, particularly when it is small compared to the sound wavelength.<sup>[177]</sup> In either case, the streaming arises as a consequence of viscous dissipation in the fluid within the Stokes (or viscous) boundary layer of thickness

$$\delta \equiv \left( \frac{2\mu}{\rho\omega} \right)^{1/2} \quad (8)$$

adjacent to the acoustic source or the oscillating body;  $\mu$  being the liquid shear viscosity.

In the case of an oscillating bubble, the streaming that ensues is referred to as microstreaming, or more specifically, cavitation microstreaming.<sup>[178]</sup> When a sound field is externally applied to a suspension of gas bubbles in an incompressible liquid, the bubbles are driven to oscillate and grow in response to the acoustic pressure that is imposed through an asymmetric rectified diffusion in which the larger influx of gas as the bubble expands during the rarefaction half cycle is greater than that flowing out during the compression half cycle.<sup>[179]</sup> At small pressure amplitudes, the response is linear and the bubble of radius  $R_0$  oscillates at its natural resonant frequency<sup>[180]</sup>

$$f_0 = \frac{\omega_0}{2\pi} = \frac{1}{2\pi R_0} \left( \frac{3\kappa p_0}{\rho} \right)^{1/2} \quad (9)$$



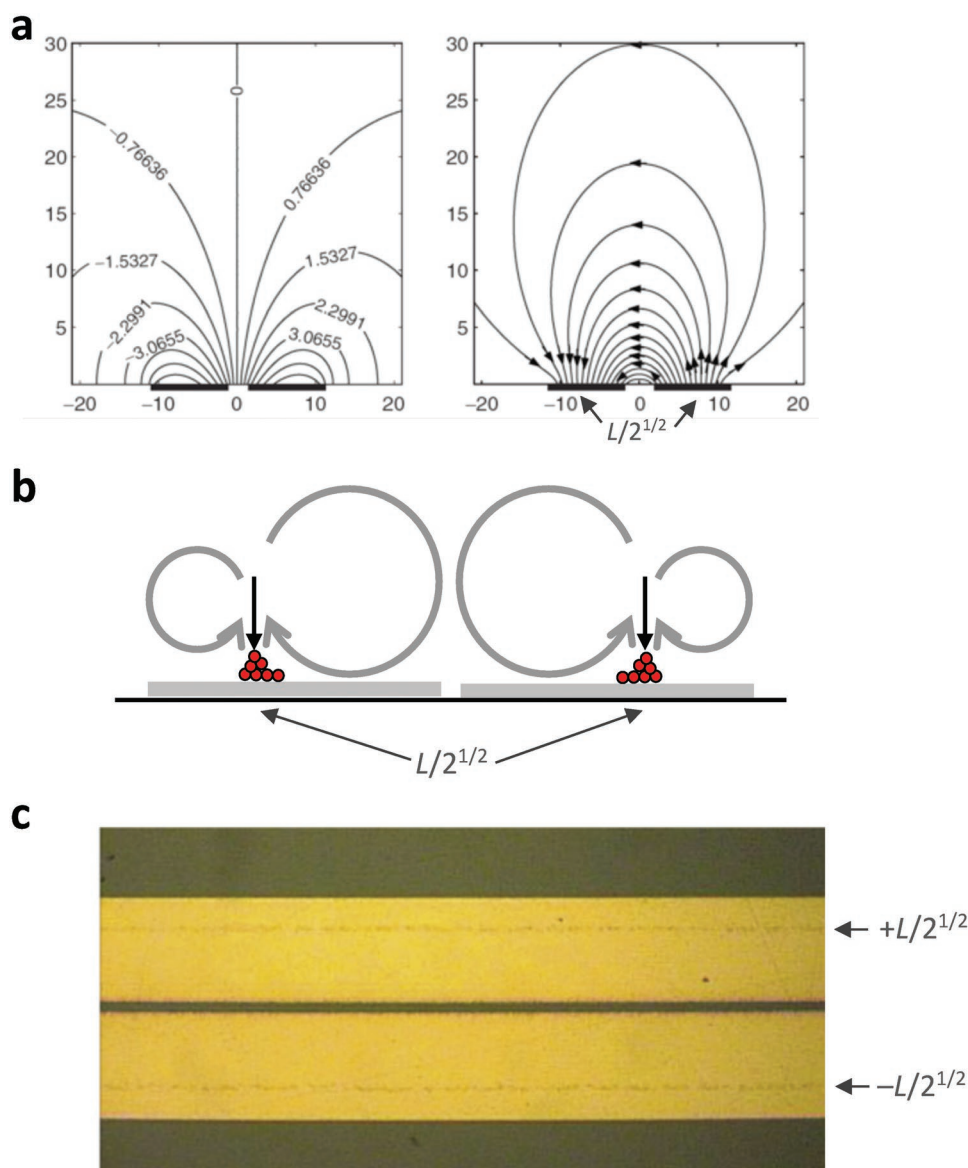


**Figure 10.** AC electrokinetic vortices. a) Equipotential (left) and electric field (right) lines associated with AC electroosmotic flow generated on symmetric co-planar electrodes due to capacitive charging at low applied frequencies; the tangential electric field can be seen to reverse its direction at  $l/2^{1/2}$  of the electrode width, giving rise to b) converging-stagnating flow that facilitates c) particle/cell (in this case, bacteria) trapping at this stagnation line along the electrode (Reproduced with permission.<sup>[162]</sup> Copyright 2010, Cambridge University Press; Reproduced with permission.<sup>[166]</sup> Copyright 2006, Canadian Society for Chemical Engineering).

in which  $p_0$  is the ambient pressure and  $\kappa$  the polytropic exponent, which equals the specific heat ratio  $\gamma$  if the pressure–volume relationship is adiabatic. As the acoustic pressure is increased, the bubble, while continuing to oscillate in a stable manner in a process known as noninertial or stable cavitation, is subject to increasing nonlinear effects<sup>[181]</sup> leading to dispersion that results in both subharmonic and superharmonic responses to the time-varying bubble radius  $R(t)$ , as governed by the Rayleigh–Plesset equation

$$R \frac{d^2 R}{dt^2} + \frac{3}{2} \left( \frac{dR}{dt} \right)^2 = - \frac{p_0}{\rho} \left[ 1 - \left( \frac{R_0}{R} \right)^{3\kappa} \right] \quad (10)$$

from which Equation (9) is recovered upon linearization about small oscillation amplitudes. Upon further increases in the acoustic pressure beyond a threshold value,<sup>[182]</sup> the bubble is subject to large oscillations to the point of collapse in what is known as inertial or transient cavitation.

The microstreaming that occurs around the bubble is a consequence of such nonlinearity, wherein the gradient in the sound field gives rise to time-averaged net motion of the fluid in the form of circulation patterns near the surface of the bubble. More specifically, primary vortices within the boundary layer adjacent to the bubble surfaces are generated, which feed outer secondary vortices with length scales on the order of the bubble dimension, with the circulation most intense when the

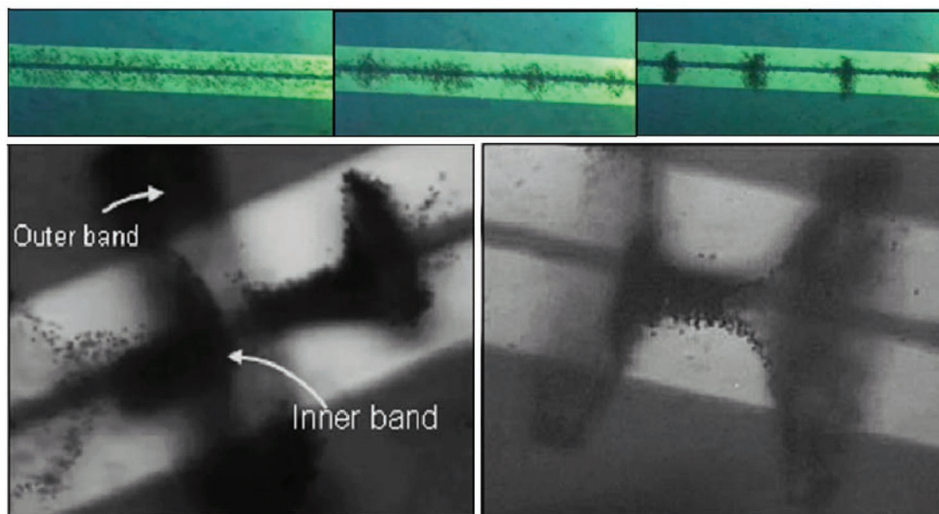


**Figure 11.** AC electrokinetic vortices. Dynamic particle banding arising from DC-biased AC electroosmotic flow vortices generated on symmetric co-planar electrodes in which the cylindrical particle structures can become unstable, leading toward their break-up into concentric bands that then merge to form conical and butterfly-like structures (Reproduced with permission.<sup>[169]</sup> Copyright 2006, American Institute of Physics).

bubble is driven to oscillate at its resonant frequency, given by Equation (9). The streaming pattern is primarily dependent on the oscillation mode, which is a function of the excitation frequency. A dipole pattern comprising two vortices, as seen in **Figure 13a**, arises, for example, when the bubble is subject to volumetric pulsations, whereas a quadrupole comprising four vortices, as observed in **Figure 13b**, manifests if the bubble undergoes translational harmonic vibration, the former being the stronger of the two.<sup>[183]</sup>

Besides being used for noncontact cleaning of various surfaces such as semiconductor wafers,<sup>[89]</sup> microstreaming has been exploited for drug delivery by enhancing convective transport of therapeutic molecules across tissue.<sup>[90,91]</sup> In microfluidic systems, bubble-induced vortices have been employed to drive micromixing<sup>[92–94]</sup> (**Figure 14**); manipulate, selectively trap, aggregate, and disperse particles;<sup>[95–97]</sup> induce cell deformation as a mechanical biomarker for disease diagnosis;<sup>[98]</sup> and as micropropulsion systems,<sup>[99]</sup> although challenges in generating and stabilizing the bubbles, pneumatically controlling their protrusion in the channel,<sup>[185]</sup> preventing their detachment—which could lead to the aggregation of the bubbles themselves, and subsequent clogging of microchannels—together with the typically large acoustic transducers required to drive the bubble oscillation and the relatively short range local streaming flows that can be generated, pose a number of practical limitations with these systems. To circumvent the disadvantages of using bubbles, it is possible to acoustically excite microposts or micropillars in their place to induce microstreaming flows,<sup>[102,103]</sup> although the other disadvantages associated with such systems remain. More recently, optical excitation of a suspension of plasmonic nanoparticles as a means to generate sound waves in the liquid via rapid expansion and contraction of both the nanoparticles and the surrounding liquid media in what is known as the photoacoustic effect, in combination with the simultaneous creation of a plasmonic–acoustic cavity due to the ablation of the nanoparticles, was demonstrated to give rise to acoustic streaming.<sup>[110,111]</sup>

More conventionally, acoustofluidic systems have primarily been driven using a variety of bulk sound waves, such as thickness mode (e.g., Lamb) waves, generated using a piezoelectric element. The undulating boundary due to the bulk substrate vibration gives rise to a number of streaming phenomena across different length scales as a consequence of the divergence in the momentum flux. Within the viscous boundary layer of Equation (8), boundary layer or Rayleigh streaming arises due to velocity continuity at the solid–liquid interface;<sup>[173,174,186,187]</sup> naturally, the boundary conditions as well as the confinement geometry has a large influence on the nature and intensity of the streaming vortices (**Figure 15**).<sup>[188,189]</sup> If the characteristic system dimension of the boundaries confining the liquid  $L$  are sufficient to support the leakage of sound waves in the fluid (i.e.,  $L \gg \lambda_f$ ),<sup>[190,191]</sup> wherein  $\lambda_f$  is the sound wavelength in the fluid at the frequency associated with that excited in the substrate, viscous dissipation and hence the attenuation of the sound wave in the bulk liquid drives a longer range flow known as Eckart streaming<sup>[107,190,192]</sup> over length scales comparable to the attenuation length

$$\beta^{-1} = \frac{\omega^2}{\rho c^3} \left( \frac{4\mu}{3} + \mu_b \right) \quad (11)$$

in which  $c$  represents the speed of sound in the fluid. To resolve the acoustic streaming pressure and velocity fields, it is necessary to carry out a perturbation expansion of the velocity, pressure and density fields about a small parameter  $\epsilon = U/c \ll 1$  in the limit of infinitesimally small amplitude sound waves, wherein  $U$  is the characteristic acoustic particle velocity.<sup>[193–195]</sup>

$$\mathbf{u} = \mathbf{u}_0 + \epsilon \mathbf{u}_1 + \epsilon^2 \mathbf{u}_2 + O(\epsilon^3) \quad (12)$$

$$p = p_0 + \epsilon p_1 + \epsilon^2 p_2 + O(\epsilon^3) \quad (13)$$

$$\rho = \rho_0 + \epsilon \rho_1 + \epsilon^2 \rho_2 + O(\epsilon^3) \quad (14)$$

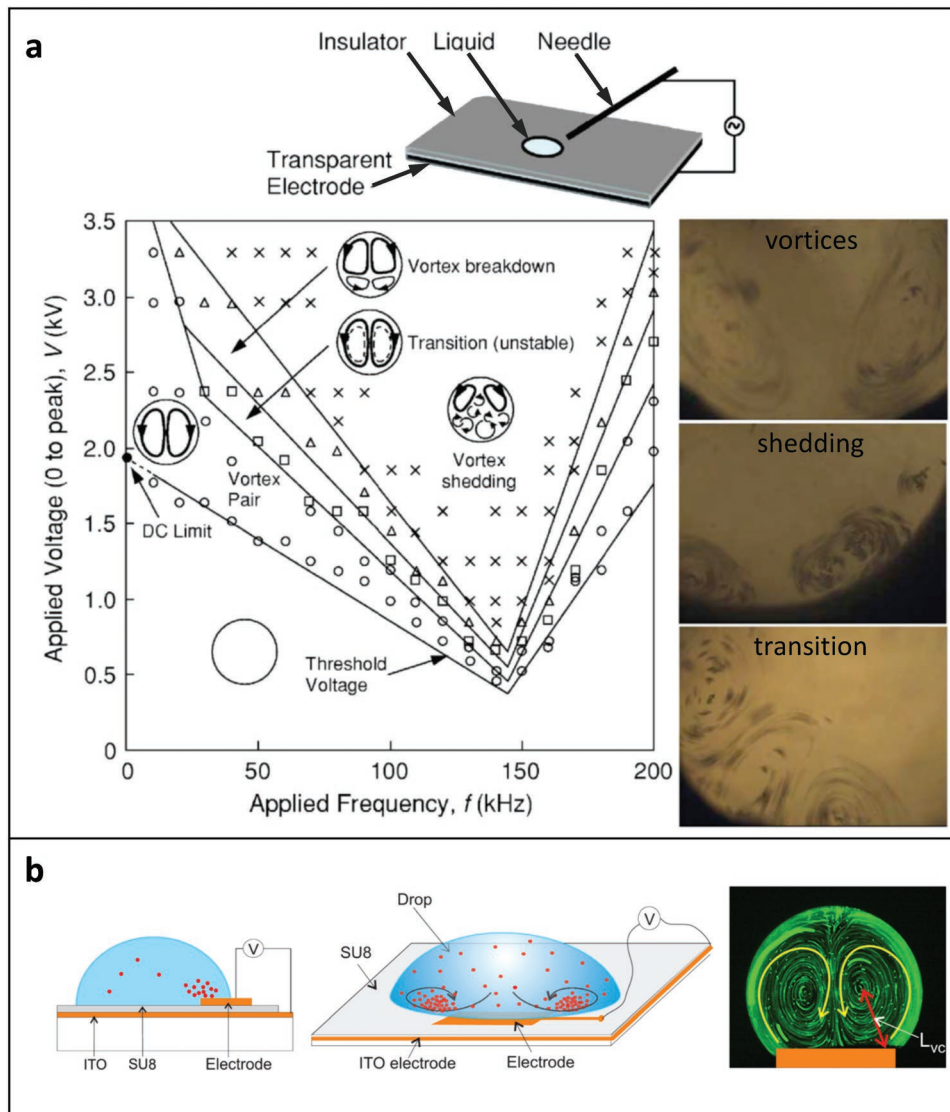


**Figure 12.** Interfacial electrokinetic vortices. a) Schematic (top), phase map (bottom left), and experimental images (bottom right) showing vortices generated at the free surface of a liquid well through ionic wind shearing (Reproduced with permission.<sup>[83]</sup> Copyright 2006, American Institute of Physics). b) Internal vortices generated in a sessile drop under AC electrowetting;  $L_{VC}$  denotes the distance between the center of the vortex and the pinned contact line (Reproduced with permission.<sup>[88]</sup> Copyright 2013, AIP Publishing LLC).

such that the equations that govern mass and momentum conservation in the fluid to first-order approximation become

$$\frac{\partial \rho_1}{\partial t} + \rho_0 (\nabla \cdot \mathbf{u})_1 = 0 \quad (15)$$

and

$$\rho_0 \frac{\partial \mathbf{u}_1}{\partial t} = -\nabla p_1 + \mu \nabla^2 \mathbf{u}_1 + \left( \mu_b + \frac{\mu}{3} \right) \nabla \nabla \cdot \mathbf{u} \quad (16)$$

respectively, and that to second-order reads

$$\frac{\partial \rho_2}{\partial t} + \nabla \cdot (\rho_0 \mathbf{u}_2) + \nabla \cdot (\rho_1 \mathbf{u}_1) = 0 \quad (17)$$

and

$$\rho_0 \frac{\partial \mathbf{u}_2}{\partial t} + \rho_1 \frac{\partial \mathbf{u}_1}{\partial t} + \rho_0 (\mathbf{u}_1 \cdot \nabla) \mathbf{u}_1 = -\nabla p_2 + \mu \nabla^2 \mathbf{u}_2 + \left( \mu_b + \frac{\mu}{3} \right) \nabla \nabla \cdot \mathbf{u}_2 \quad (18)$$

respectively, wherein the subscript 0 refers to equilibrium properties associated with ambient conditions, and the subscripts 1 and 2 to the first- and second-order fields, respectively. Closure to the above set of equations is then obtained through a thermodynamic equation of state, which, to first- and second-order approximation, are given, for example for an adiabatic process (in which the entropy  $s = s_0$ ), by

$$p_1 = c_0^2 \rho_1 \quad (19)$$

and



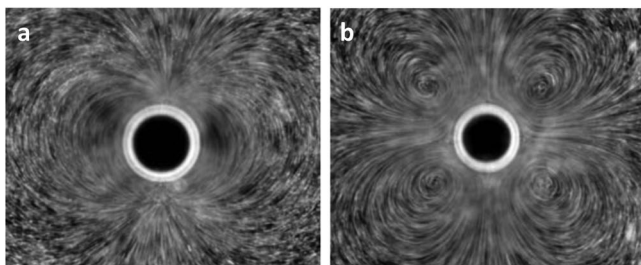


**Figure 13.** Bubble cavitation microstreaming. a) Dipole and b) quadrupole vortex generation around a bubble subjected to volumetric oscillation and translational harmonic vibration, respectively (Reproduced with permission.<sup>[184]</sup> Copyright 2007, Cambridge University Press).

$$p_2 = \frac{c_0^2}{\rho_0} \left( \frac{1}{2} \frac{B}{A} \rho_1^2 + \rho_0 \rho_2 \right) \quad (20)$$

respectively, in which  $A = \rho_0 c_0^2$  and  $B = \rho_0^2 (\partial c^2 / \partial \rho)_s$  are the adiabatic bulk elastic and nonlinear moduli. Time averaging of the second-order equations  $\langle a \rangle = \lim_{T \rightarrow \infty} (1/T) \int_0^T a(t) dt$  where  $T = n/f$  ( $n = 1, 2, 3, \dots$ ), then yields a time-averaged effective body force density

$$\begin{aligned} \mathbf{F}_{dc} &\approx \nabla p_{dc} - \mu \nabla^2 \mathbf{u}_{dc} \\ &= -\frac{1}{c_0^2} \left\langle p_1 \frac{\partial \mathbf{u}_1}{\partial t} \right\rangle - \rho_0 \langle (\mathbf{u}_1 \cdot \nabla) \mathbf{u}_1 \rangle - \frac{1}{c_0^2 \rho_0} \left( \mu_B + \frac{\mu}{3} \right) \nabla \nabla \cdot \langle p_1 \mathbf{u}_1 \rangle \end{aligned} \quad (22)$$

or, in terms of the vorticity  $\Omega = \frac{1}{2} \nabla \times \mathbf{u}_1$ ,

$$\mathbf{F}_{dc} = -\frac{1}{c_0^2} \left\langle p_1 \frac{\partial \mathbf{u}_1}{\partial t} \right\rangle - \frac{\rho_0}{2} \langle \nabla (\mathbf{u}_1 \cdot \mathbf{u}_1) \rangle + 2\rho_0 \langle \mathbf{u}_1 \times \Omega \rangle \quad (23)$$

Alternatively, it is also possible to define the strength of the vorticity source by taking the curl of the body force expression in Equation (22).

In practice, piezoelectric transducers in various configurations, either directly by vibrating the fluid itself,<sup>[112–115]</sup> or indirectly by exciting the oscillation of surfaces in contact with the fluid (such as cylinders<sup>[100]</sup> or pipettes,<sup>[101]</sup> membranes,<sup>[106]</sup> resonant cavities,<sup>[107,108]</sup> or even the microchannel wall protrusions<sup>[104]</sup>

in Section 2.2 or the reaction chamber of the microfluidic chip itself<sup>[105]</sup>), have been employed to transmit bulk acoustic waves into the fluid in order to generate acoustic streaming in microfluidic devices for various applications. In the case of a sessile drop atop the piezoelectric device, for example, a poloidal flow arises if the length over which the sound wave in the substrate attenuates under the damping effect of the drop

$$\alpha^{-1} \approx \frac{\rho c}{\rho_s c_s \lambda_s} \quad (24)$$

as well as the length over which the sound waves generated in the liquid responsible for the Eckart streaming attenuates  $\beta^{-1}$  (Equation (11)), do not exceed the drop radius;  $\rho_s$  is the density of the piezoelectric substrate, and  $c_s$  and  $\lambda_s$  are the corresponding sound speed and wavelength in the substrate, respectively. This, in turn, drives the formation of a toroidal particle ring in the case of a particle-laden droplet (Figure 16).<sup>[114,115]</sup> Additionally, it has also been shown that the placement of a piezoelectric element at an offset position beneath a chamber of a 24-well microarray titer plate can be used to transmit the bulk vibration to the base of a well with the aid of a liquid couplant so as to generate a vortical flow in the chamber, although the complexity of the setup—in particular, the mounting of the element at an angle to the well and the electrical connections required to each element (one is required beneath each well)—makes realization difficult, and, as such, addressability of each well in the entire microarray plate was not demonstrated.<sup>[109]</sup> A more elegant solution employing a hybrid combination of surface and bulk waves for on-demand individual, sequential, and simultaneous addressability of all the wells in a 96-well microarray plate will be discussed below.<sup>[139]</sup>

Surface waves, in particular, surface acoustic waves (SAWs), which due to their higher frequencies (>10 MHz) and hence shorter wavelengths  $\lambda_a \ll h$ , are confined to the surface of the piezoelectric substrate of thickness  $h$  in contrast to the aforementioned bulk acoustic waves where  $\lambda_a > h$  ( $\lambda_a$  being the wavelength of the specific acoustic wave in the substrate), are an attractive alternative that have been shown to be particularly efficient in driving a wide range of microfluidic flows.<sup>[196–199]</sup> In addition to their ability to efficiently generate boundary layer

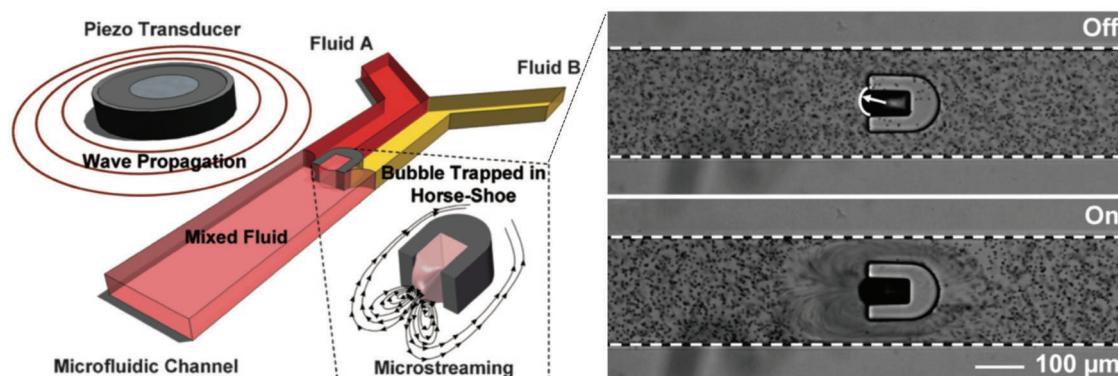


**Figure 14.** Microfluidic bubble mixer. The microstreaming arising from the vibration of an air bubble trapped in a horse-shoe structure that is fabricated into a microchannel at resonance using a piezoelectric element is employed for micromixing of two laminar streams (Reproduced with permission.<sup>[94]</sup> Copyright 2009, The Royal Society of Chemistry).

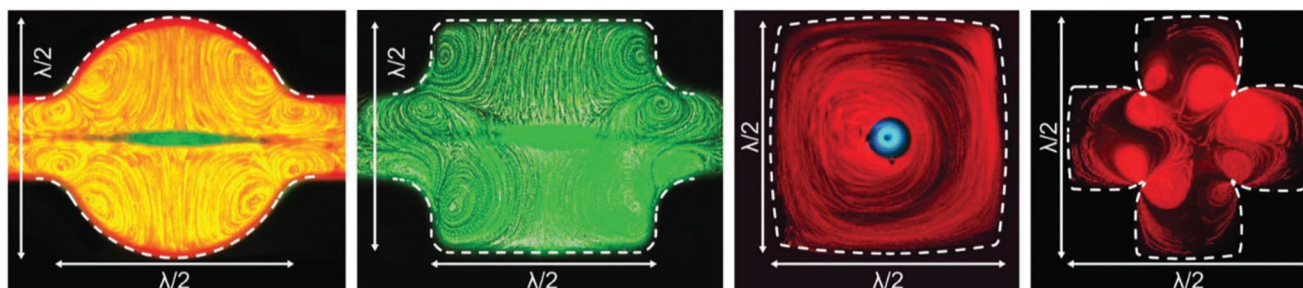


**Figure 15.** Acoustic streaming. Examples of Rayleigh streaming in different microfluidic resonant cavities of widths between 300 and 350  $\mu\text{m}$ , excited by bulk acoustic waves at frequencies between 2.1 and 2.6 MHz (Reproduced with permission.<sup>[107]</sup> Copyright 2012, The Royal Society of Chemistry).

(Schlichting) and Rayleigh streaming vortices similar to their bulk counterparts,<sup>[190,200,201]</sup> the leakage of the acoustic energy into the fluid arising from wave diffraction into the fluid—a consequence of the mismatch in the sound speeds in the piezoelectric chip and the liquid—gives rise to the propagation of sound waves in the liquid whose attenuation leads to the same long range Eckart streaming discussed above.<sup>[202–205]</sup> As in a sessile drop, the generation of vortices in a microchannel is dependent on the relative ratio between the characteristic system dimension and the attenuation length, which is related to the SAW frequency (Equation (11)) and sound wavelength in the liquid  $\lambda_f$ . If the microchannel dimension is smaller than  $\lambda_f$ , there is insufficient length over which the sound wave in the liquid propagates and hence attenuates, and unidirectional flow—useful for micropumping applications—ensues, albeit with the possibility for the generation of localized vortices confined within the boundary layer due to Schlichting and Rayleigh streaming.<sup>[205,206]</sup> On the other hand, microchannel dimensions greater than  $\lambda_f$  allows Eckart streaming vortices to be sustained, both longitudinally<sup>[128]</sup> (Figure 17), as well as transverse to the main flow direction in the channel.<sup>[136,207–210]</sup>

To generate an azimuthal microfluidic centrifugation flow either in a liquid drop or chamber atop the piezoelectric substrate (Figure 18a), on the other hand, it is necessary to break the symmetry of the planar SAW wave. This can be achieved, for example, by offsetting the interdigitated transducer(s) used to generate the SAW(s) with respect to the position of the drop,

by introducing an asymmetric cut to the SAW chip such that the reflection of the SAW at its edges varies transversely across the drop, or, by absorbing part of the SAW prior to its reflection, as illustrated in Figure 18b.<sup>[118,119,124,125]</sup> Given that the flow is driven primarily as a consequence of the attenuation of the sound wave in the liquid, the vortex dimension is naturally inversely proportional to the frequency. Local recirculation at far shorter length scales than that of the drop are then observed if GHz frequencies with attenuation lengths typically below 100  $\mu\text{m}$  are employed.<sup>[122]</sup>

In any case, such on-chip microcentrifugation flows were subsequently demonstrated as powerful tools to drive micro-mixing<sup>[211–213]</sup> as well as sample and particle preconcentration. In the latter, it was shown to be possible to either induce particle or molecular aggregation into a spot—either at the free surface as a consequence of shear induced migration,<sup>[118,119]</sup> or in the bulk due to boundary layer effects on the secondary meridional recirculation;<sup>[120]</sup> such an ability to drive particle or solute agglomeration is particularly useful for the separation of red blood cells from plasma,<sup>[118,214]</sup> sample/analyte preconcentration,<sup>[118,119]</sup> particle sorting/partitioning,<sup>[121]</sup> cell agglomeration<sup>[123]</sup> and crystallization,<sup>[126]</sup> among other applications (alternatively, the opposite effect, i.e., particle/solute dispersion can simply be achieved by increasing the input power to the device<sup>[118]</sup>). In SAW-driven cell agglomeration, for example, it was shown that the size of the agglomerates, which could control the size of spheroidal body formation, for example, can be tuned through the SAW

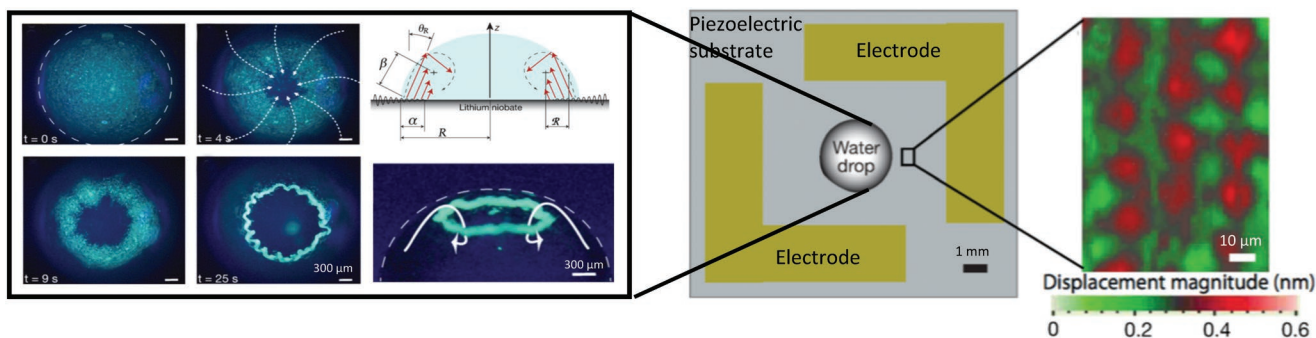


**Figure 16.** Vortices driven by bulk acoustic wave excitation. Poloidal flow and toroidal particle ring generation in a sessile drop as a consequence of Lamb wave excitation on a piezoelectric substrate; such a flow arises as a consequence of the attenuation of the sound waves in the drop when both the attenuation length of the Lamb wave in the substrate  $\alpha^{-1}$  due to damping in the presence of the drop, as well as the attenuation of the sound wave propagation in the liquid  $\beta^{-1}$  due to the viscosity of the liquid, do not exceed the drop radius  $R$  (Reproduced with permission.<sup>[114]</sup> Copyright 2014, American Chemical Society).

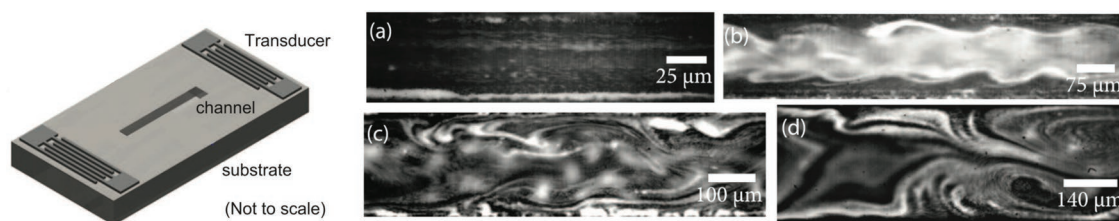


**Figure 17.** Acoustic streaming driven by SAWs in microchannels. The acoustic streaming flow that arises in a microchannel cut into a SAW substrate (left)—a consequence of the leakage of the SAW energy into the fluid in the channel to produce propagating bulk sound waves—is shown to be dependent on the microchannel width  $W$  relative to the sound wavelength in the liquid  $\lambda_f$  (right). In this case, the SAW frequency is 20 MHz and hence  $\lambda_f = 73 \mu\text{m}$  at this frequency; it can be seen that the unidirectional flow that arises in narrow channels where  $W < \lambda_f$  as a result of insufficient lengths over which the sound wave can attenuate before reflecting at the channel boundaries (image a) gives way to flows that are increasing in vorticity (images b–d) as  $W$  increases beyond  $\lambda_f$  (Reproduced with permission.<sup>[128]</sup> Copyright 2009, EPLA).

power.<sup>[123]</sup> Additionally, the microfluidic centrifugation flows were also demonstrated to be a versatile means for rotating miniature discs on which microfluidic channels can be patterned to carry out a host of different operations and assays—a substantially smaller (a few millimeters as opposed to many centimeters in diameter) and more compact, miniaturized, integrated, and low cost version of the lab-on-a-CD.<sup>[137,138]</sup>

SAWs, as well as thickness-mode bulk waves, can also be generated on thin piezoelectric films (the latter being known as thin film bulk acoustic resonators, and has the advantage of overcoming challenges associated with fabricating interdigitated transducers with micron or submicron widths and thicknesses necessary to generate SAWs at higher (e.g., GHz) frequencies),<sup>[215–217]</sup> on which similar azimuthal microfluidic centrifugation flows can be effected. In addition to demonstrating the microvortical flow arising from these devices for various applications, including hydrodynamic particle trapping,<sup>[218]</sup> biomolecular concentration<sup>[219]</sup> and the shearing of polyelectrolyte films for drug release,<sup>[220]</sup> the piezoelectric films can be overlaid onto regular substrates so as to circumvent the need for the piezoelectric substrate as well as to facilitate microfluidic operations on flexible substrates.<sup>[221–225]</sup> To however separate the actuator

from the microfluidic components, so as to enable reuse of the actuator (i.e., the piezoelectric chip) while facilitating a disposable option for the microfluidic chip, it is necessary to transmit the SAW vibration through a liquid couplant into a superstrate (e.g., a low-cost and hence disposable chip on which the microfluidic operations are to be carried out as opposed to the reusable higher-cost piezoelectric substrate to drive the microfluidic actuation), as first shown by Hodgson et al.,<sup>[132]</sup> or even a capillary tube.<sup>[136]</sup> In place of the superstrate, a phononic crystal can also be used, wherein it was shown that introducing a defect allows the creation of a bandgap that permits symmetry breaking of the vibration in the phononic crystal so as to drive the azimuthal microfluidic centrifugation flow on the crystal superstrate in a similar way to the strategies shown in Figure 18b for generating asymmetric SAWs.<sup>[134,135]</sup> We note, however, that in all of these cases, the vibration that is generated on the superstrate, capillary tube or phononic crystal through the coupling layer no longer consists of a SAW but is rather a bulk wave that exists throughout the thickness of the material.<sup>[132]</sup> To retain a SAW on the superstrate, which is considerably more efficient in driving microfluidic actuation compared to bulk acoustic waves, a simple modification

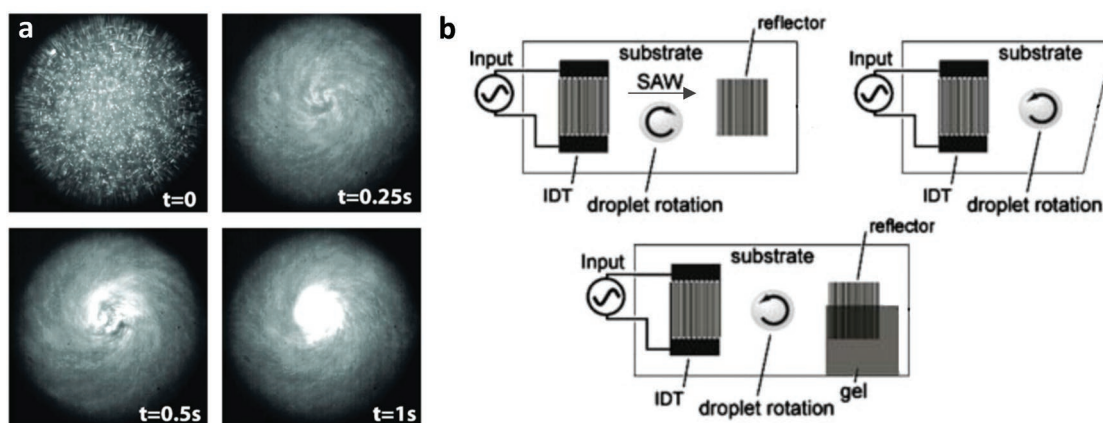


**Figure 18.** SAW-driven microfluidic centrifugation flow. a) Azimuthal recirculating flow, seen here to drive rapid concentration of fluorescent particles into a focal spot, can be generated in a sessile drop or microwell by b) breaking the symmetry of the planar SAW through a number of ways, for example, by offsetting the drop such that part of it lies outside the SAW irradiation pathway (top left), introducing an asymmetric cut such that the reflection of the SAW at the device edges is nonuniform across the drop (top right), or, by absorbing part of the SAW to prevent its reflection back to the drop (bottom); the arrow denotes the propagation direction of the SAW (Reproduced with permission.<sup>[119]</sup> Copyright 2008, American Institute of Physics; and [118] Copyright 2007, Springer Science + Business Media LLC).



involving the sputtering of a thin gold layer on the superstrate was demonstrated to be sufficient in suppressing the bulk wave in lieu of a SAW on the superstrate as a consequence of wave reflections through the material.<sup>[133]</sup>

The transmission of the acoustic energy associated with the SAW through the liquid couplant is also useful for flow actuation in the microwells of a microarray titer plate. In order to overcome the limitations of not only bulk acoustic wave vibration described above<sup>[109]</sup> as well as that of the SAW—namely, the physical space required for the interdigitated transducers which interfere with the placement of the microwells above them, the use of a hybrid surface and bulk wave in the form of surface reflected bulk waves (SRBW) has been proposed by exploiting the intermediate asymptotic region between the surface and bulk wave limits where  $\lambda_a \sim h$ .<sup>[140]</sup> This allowed the transducers to be patterned on the underside of the substrate through whose thickness the acoustic energy can be transmitted so that it couples into the liquid couplant and hence the microwell from above. This was then demonstrated for generating microvortexing in the microwells—individually, sequentially or simultaneously—on-demand for flexible addressability of the microwell titer plates as an attractive alternative to that in ref. [109] (Figure 19).<sup>[139]</sup>

Another interesting concept involves the generation of an acoustic radiation torque and hence an ultrasonic vortex beam<sup>[116]</sup> in the liquid through the transfer of acoustic orbital angular momentum whose attenuation in the liquid gives rise to rotational flow. This was realized through an array of curved piezoelectric transducers, each of which are sequentially excited

via the successive application of a sinusoidal wave to each,<sup>[117]</sup> and, more recently, through the generation of swirling SAWs with the use of a concomitant array of interdigitated transducers that are also sequentially activated, or a spiral electrode, although the anisotropy of the piezoelectric substrate needs to be carefully compensated for in the transducer design or the input signal in the latter.<sup>[129–131]</sup>

### 3.3. Thermal Actuation

Convective currents due to density gradients (i.e., Rayleigh–Bénard convection<sup>[141,142]</sup>), or, more broadly, substrate energy gradients<sup>[143]</sup> (the electrocapillary effect, or electrowetting (Section 3.1), being one example of this), can be generated by introducing thermal differences within the fluid or along the substrate, although localized heating elements (or, in the latter, surface chemical patterning, for example) may not always be simple to integrate into microfluidic devices; moreover, control of the heating and actuation can often be difficult, and neither is the system easily reconfigurable. In open microfluidic systems where a free surface is present, e.g., a drop, it is also possible to exploit Marangoni (i.e., interfacial) stresses arising from surface tension gradients, induced either via the addition of surface active agents (e.g., surfactants), by imposing thermal gradients (i.e., the thermocapillary effect), or simply through evaporation.<sup>[143–145]</sup> Like surfactants or chemical patterning, whose incorporation can alter the fluid properties, a disadvantage of thermal actuation is that it is usually a one-off,

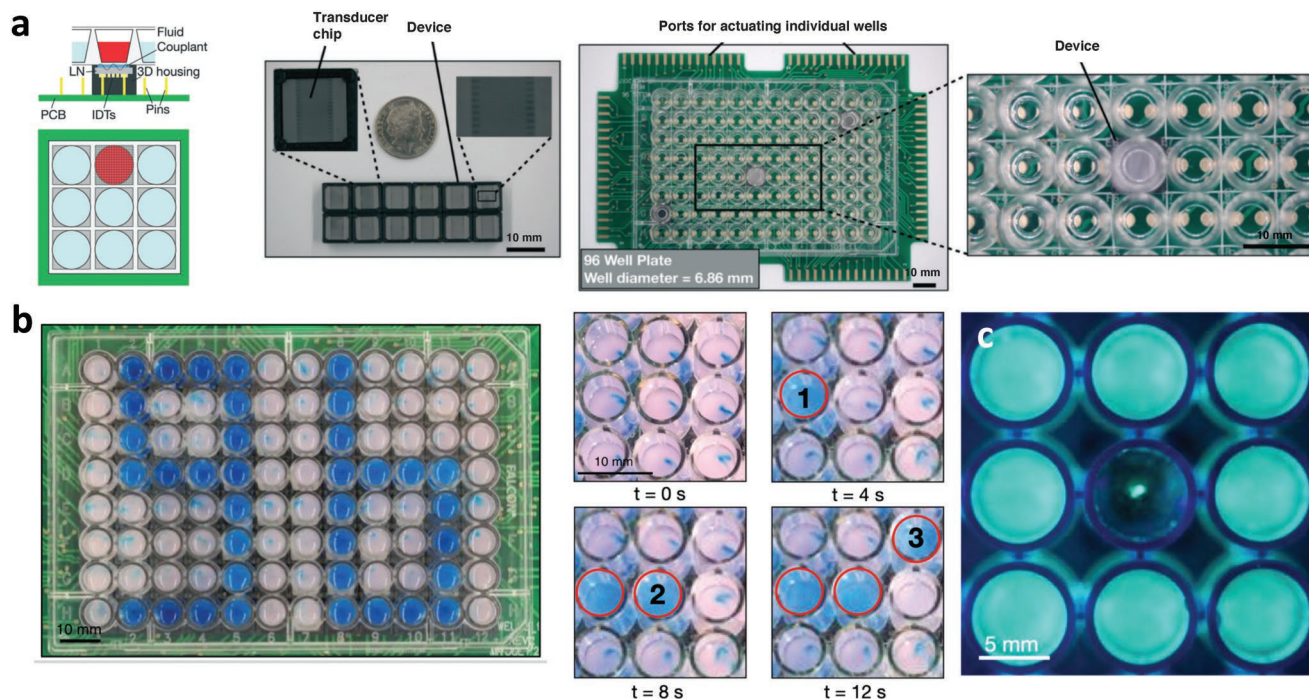


**Figure 19.** Vortical flows generated on-demand in individual microwells of a 96-well microarray titer plate. The coupling of hybrid surface and bulk waves through a liquid layer into microwells in the microarray titer plate from individual piezoelectric devices powered and controlled by a printed circuit board from beneath is employed to individually, sequentially, or simultaneously address each microwell to effect a) micromixing (the numbers indicate the sequence by which each microwell is activated), or b) particle concentration (Reproduced with permission.<sup>[139]</sup> Copyright 2018, The Royal Society of Chemistry.

irreversible effect; in other words, the surfactant or heat, once added to the system, cannot be easily “removed,” and more has to be added to continually drive the actuation. Further, we also note that heating the fluid in all of these systems may not be desirable, particularly where biological samples are concerned.

These limitations notwithstanding, local fluid recirculation can also be generated thermally via other means, for example, via the photoacoustic effect discussed previously in Section 3.2. Alternatively, local Joule heating as a consequence of the applied electric field,<sup>[73–76]</sup> or externally imposed, for example using a laser,<sup>[77–79]</sup> can give rise to temperature gradients in the fluid, that can also result in nonuniform permittivity  $\epsilon$  and conductivity  $\sigma$ , and hence an accumulation of space charge  $\rho_e$  that manifests as a time-averaged (for AC fields) Maxwell body force<sup>[226]</sup>

$$\langle F_e \rangle = \frac{1}{2} \operatorname{Re} \left[ \frac{\sigma \epsilon}{\sigma + i\omega \epsilon} \left\{ \frac{1}{\epsilon} \left( \frac{\partial \epsilon}{\partial T} \right) - \frac{1}{\sigma} \left( \frac{\partial \sigma}{\partial T} \right) \right\} (\nabla T \cdot \mathbf{E}) \mathbf{E}^* - \frac{1}{2} \frac{\partial \epsilon}{\partial T} |\mathbf{E}|^2 \nabla T \right] \quad (25)$$

in a phenomena known as the electrothermal effect. In the above,  $\sigma$  is the conductivity of the fluid,  $T$  the temperature and  $\mathbf{E}$  the electric field, the asterisk  $*$  denoting its complex conjugate and  $\operatorname{Re}[\cdot]$  the real part of the term in the parenthesis. The first term on the right of Equation (25) constitutes the Coulombic force, which dominates at low frequencies whereas the second constitutes the dielectric force, which dominates at high frequencies. Since the local temperature gradient  $\nabla T$  scales as  $\sigma V^2 / \kappa$  from an order-of-magnitude approximation of the energy conservation equation, in which  $V$  is the applied voltage and  $\kappa$  the thermal conductivity of the fluid, it then follows that  $\langle F_e \rangle \sim E^2 \nabla T \sim E^4$ . Such localized temperature gradients have been shown to give rise to a vortical flow, which can be combined with dielectrophoretic trapping to enable particle aggregation and trapping (Figure 20).<sup>[78,80–82]</sup>

### 3.4. Mechanical and Pneumatic Systems

Mechanical actuation using micro-electromechanical systems (MEMS), for example, the rotating microimpellers fabricated in SU-8 and housed within a pump chamber, and driven either electrically,<sup>[146]</sup> through rotational vibration displacements

induced by an asymmetric SAW with which the impeller is directly in contact with,<sup>[147]</sup> or even by the aforementioned SAW-generated azimuthal microfluidic centrifugation flow itself,<sup>[148]</sup> for example, are effective ways for generating vortical flows, but the use of rotors can be subject to degradation in performance and reliability due to issues associated with clogging and wear as with all mechanically moving components at these scales. Pneumatic means, for example, the generation of an airflow to shear the surface of a liquid contained in a microchamber to induce it to rotate<sup>[149]</sup> in the same way as that driven by ionic wind (Section 3.1),<sup>[83–87]</sup> have also been proposed, although such systems are often hampered by the incompatibilities in integrating large compressed air sources or pneumatic pumps with small scale microfluidic devices.

## 4. Summary

We have reviewed the state-of-the-art to date related to the various methods that have been reported in the literature for the generation of centrifugal flows in microfluidic devices. Passive systems, which rely on the incorporation of geometrical or topological features to promote flow detachment from channel boundaries, while benefitting from simplicity and potentially low-costs, often require considerable inertia within the system due to the large pressure drops generated by these features, thereby necessitating large pumps which are not always amenable to miniaturization and integration into the microfluidic device. Active systems, on the other hand, rely on the use of external forces—for example that arising from applied electric, acoustic, optic, and magnetic fields—to drive rotation in the system, and can be extremely versatile and powerful for generating intense vortices in various microchannel configurations. The need for power sources to supply these fields can however be restrictive for integration if these cannot be readily integrated, for instance, due to their complexity and size.

The field of microfluidic actuation, including the developments to date for the generation of microfluidic centrifugal flows, has considerably matured over the last decade with now many different mechanisms available, as detailed in the current review. We thus anticipate future work to evolve toward addressing the challenge of incorporating not just the microfluidic centrifugation step, but also the various individual unit operations (including those associated with the upstream

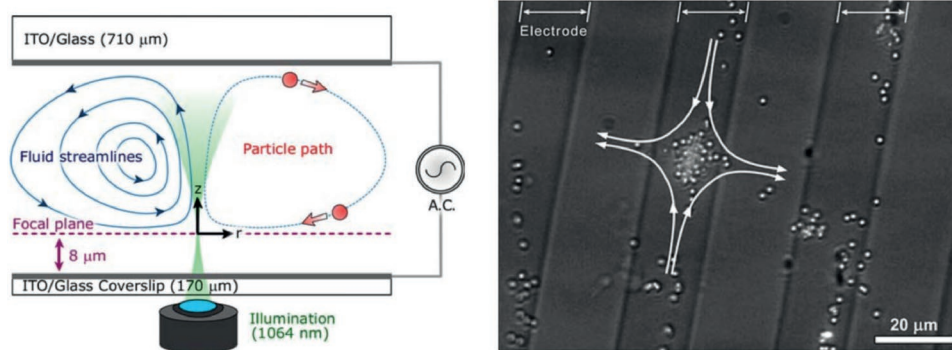


**Figure 20.** Electrothermal vortices. Schematic depiction of the experimental setup (left) and image showing the vortices generated under localized temperature gradients (right) induced optically using a focussed laser beam (Reproduced with permission.<sup>[78]</sup> Copyright 2008, Springer-Verlag).

actuation and downstream detection components) together with the chipscale assay into a seamless, integrated, and miniaturized device for completely portable and handheld operation, i.e., a true lab-on-a-chip (as opposed to a “chip-in-a-lab”<sup>[227]</sup>). In our opinion, this remains an unmet but realizable goal.<sup>[3]</sup>

## Acknowledgements

L.Y.Y. is grateful for support from the Australian Research Council through Discovery Project grant DP170101061.

## Conflict of Interest

The authors declare no conflict of interest.

## Keywords

concentration, microcentrifugation, recirculation, rotation, separation, vortex

Received: July 8, 2019

Revised: August 20, 2019

Published online: September 19, 2019

- [1] C. Huygens, *Oeuvres Complètes* **1673**, XVI, 255.
- [2] J. Kim, M. Johnson, P. Hill, B. K. Gale, *Integr. Biol.* **2009**, *1*, 574.
- [3] L. Y. Yeo, H.-C. Chang, P. P. Y. Chan, J. R. Friend, *Small* **2011**, *7*, 12.
- [4] E. K. Sackmann, A. L. Fulton, D. J. Beebe, *Nature* **2015**, *507*, 181.
- [5] F. Cui, M. Rhee, A. Singh, A. Tripathi, *Annu. Rev. Biomed. Eng.* **2015**, *17*, 267.
- [6] D. Di Carlo, *Lab Chip* **2009**, *9*, 3038.
- [7] H. Amini, W. Lee, D. Di Carlo, *Lab Chip* **2014**, *14*, 2739.
- [8] H. W. Hou, M. E. Warkiani, B. L. Khoo, Z. R. Li, R. A. Soo, D. S.-W. Tan, W.-T. Lim, J. Han, A. A. S. Bhagat, C. T. Lim, *Sci. Rep.* **2013**, *3*, 1259.
- [9] G.-Y. Kim, J.-I. Han, J.-K. Park, *BioChip J.* **2018**, *12*, 257.
- [10] J. Zhang, S. Yan, D. Yuan, G. Alici, N.-T. Nguyen, M. E. Warkiani, W. Li, *Lab Chip* **2016**, *16*, 10.
- [11] W. Al-Faqheri, T. H. G. Thio, M. A. Qasaimeh, A. Dietzel, M. Madou, A. Al-Halhouli, *Microfluid. Nanofluid.* **2017**, *21*, 102.
- [12] A. J. Chung, *BioChip J.* **2019**, *13*, 53.
- [13] M. Madou, J. Zoval, G. Jia, H. Kido, J. Kim, N. Kim, *Annu. Rev. Biomed. Eng.* **2006**, *8*, 601.
- [14] R. Gorkin, J. Park, J. Siegrist, M. Amasia, B. S. Lee, J.-M. Park, J. Kim, H. Kim, M. Madou, Y.-K. Cho, *Lab Chip* **2010**, *10*, 1758.
- [15] M. Tang, G. Wang, S.-K. Kong, H.-P. Ho, *Micromachines* **2016**, *7*, 26.
- [16] J. Gilmore, M. Islam, R. Martinez-Duarte, *Micromachines* **2016**, *7*, 52.
- [17] L. X. Kong, A. Perebikovsky, J. Moebius, L. Kulinsky, M. Madou, *J. Lab. Autom.* **2016**, *21*, 323.
- [18] W. H. Chong, Y. Huang, T. N. Wong, K. T. Ooi, G.-P. Zhu, *Adv. Mater. Technol.* **2018**, *3*, 1700312.
- [19] J. P. Shelby, D. S. Lim, J. S. Kuo, D. T. Chiu, *Nature* **2003**, *425*, 38.
- [20] D. T. Chiu, *Anal. Bioanal. Chem.* **2007**, *387*, 17.
- [21] Z. T. F. Yu, Y.-K. Lee, M. Wong, Y. Zohar, *J. Microelectromech. Syst.* **2005**, *14*, 1386.
- [22] B. H. Kwon, H. H. Kim, J. H. Park, D. H. Yoon, M. C. Kim, S. Sheard, K. Morten, J. S. Go, *Jpn. J. Appl. Phys.* **2013**, *52*, 026601.
- [23] H. J. Jeon, D. I. Kim, M. J. Kim, X. D. Nguyen, D. H. Park, J. S. Go, *J. Micromech. Microeng.* **2015**, *25*, 114001.
- [24] J. H. Lee, J. B. Ha, Y. K. Bahk, S. H. Yoon, T. Arakawa, J. S. Ko, B. S. Shin, S. Shoji, J. S. Go, *Sens. Actuators, B* **2008**, *132*, 525.
- [25] A. J. Mach, J. H. Kim, A. Arshi, S. C. Hur, D. Di Carlo, *Lab Chip* **2011**, *11*, 2827.
- [26] H. Yun, S. C. Hur, *Lab Chip* **2013**, *7*, 2764.
- [27] X. Wang, J. Zhou, I. Papautsky, *Biomicrofluidics* **2013**, *7*, 044119.
- [28] C. Renier, E. Pao, J. Che, H. E. Liu, C. A. Lemaire, M. Matsumoto, M. Triboulet, S. Srivinas, S. S. Jeffrey, M. Rettig, R. P. Kulkarni, D. Di Carlo, E. Sollier-Christen, *npj Precis. Oncol.* **2017**, *1*, 15.
- [29] S. C. Hur, A. J. Mach, D. Di Carlo, *Biomicrofluidics* **2011**, *5*, 022206.
- [30] E. Sollier, D. E. Go, J. Che, D. R. Gossett, S. O’Byrne, W. M. Weaver, N. Kummer, M. Rettig, J. Goldman, N. Nickols, S. McCloskey, R. P. Kulkarni, D. Di Carlo, *Lab Chip* **2014**, *14*, 63.
- [31] M. Dhar, J. Wong, A. Karimi, J. Che, C. Renier, M. Matsumoto, M. Triboulet, E. B. Garon, J. W. Goldman, M. B. Rettig, S. S. Jeffrey, R. P. Kulkarni, E. Sollier, D. Di Carlo, *Biomicrofluidics* **2015**, *9*, 064116.
- [32] P. E. Arratia, C. C. Thomas, J. Diorio, J. P. Gollub, *Phys. Rev. Lett.* **2006**, *96*, 144502.
- [33] L. Rodd, J. Cooper-White, D. Boger, G. McKinley, *J. Non-Newtonian Fluid Mech.* **2007**, *143*, 170.
- [34] S. Gulati, S. J. Muller, D. Liepmann, *J. Non-Newtonian Fluid Mech.* **2008**, *155*, 51.
- [35] S. J. Haward, Z. Li, D. Lighter, B. Thomas, J. A. Odella, X.-F. Yuan, *J. Non-Newtonian Fluid Mech.* **2010**, *165*, 1654.
- [36] M. Y. Hwang, H. Mohammadigoushki, S. J. Muller, *Phys. Rev. Fluids* **2017**, *2*, 043303.
- [37] M. Frankowski, J. Theisen, A. Kummrow, P. Simon, H. Ragusch, N. Bock, M. Schmidt, J. Neukammer, *Sensors* **2013**, *13*, 4674.
- [38] A. Haller, A. Spittler, L. Brandhoff, H. Zirath, D. Puchberger-Engel, F. Keplinger, M. J. Vellekoop, *Micromachines* **2015**, *6*, 239.
- [39] C.-H. D. Tsai, T. Takayama, Y. Shimozyo, T. Akai, M. Kaneko, *Biomicrofluidics* **2018**, *12*, 034114.
- [40] A. P. Sudarsan, V. M. Ugaz, *Proc. Natl. Acad. Sci. USA* **2006**, *103*, 7228.
- [41] R. H. Liu, M. A. Stremmer, K. V. Sharp, M. G. Olsen, J. G. Santiago, R. J. Adrian, H. Aref, D. J. Beebe, *J. Microelectromech. Syst.* **2000**, *9*, 190.
- [42] D. S. Kim, S. H. Lee, T. H. Kwon, C. H. Ahn, *Lab Chip* **2005**, *5*, 739.
- [43] T. G. Kang, M. K. Singh, P. D. Anderson, H. E. H. Meijer, *Microfluid. Nanofluid.* **2009**, *7*, 783.
- [44] D. Di Carlo, D. Irimia, R. G. Tompkins, M. Toner, *Proc. Natl. Acad. Sci. USA* **2007**, *104*, 18892.
- [45] J. Wang, Y. Zhan, V. M. Ugaz, C. Lu, *Lab Chip* **2010**, *10*, 2057.
- [46] N. Nivedita, P. Ligrani, I. Papautsky, *Sci. Rep.* **2017**, *7*, 44072.
- [47] J. M. Martel, M. Toner, *Phys. Fluids* **2012**, *24*, 032001.
- [48] V. Mengers, J. Josseland, H. H. Girault, *Anal. Chem.* **2002**, *74*, 4279.
- [49] V. H. Lieu, T. A. House, D. T. Schwartz, *Anal. Chem.* **2012**, *84*, 1963.
- [50] H. Amini, E. Sollier, M. Masaeli, Y. Xie, B. Ganapathysubramanian, H. A. Stone, D. Di Carlo, *Nat. Commun.* **2013**, *4*, 1826.
- [51] A. Renfer, M. K. Tiwari, F. Meyer, F. Brunschweiler, B. Michel, D. Poulikakos, *Microfluid. Nanofluid.* **2013**, *15*, 231.
- [52] J. A. Jarrell, A. A. Twite, K. H. W. J. Lau, M. N. Kashani, A. A. Lievano, J. Acevedo, C. Priest, J. Nieva, D. Gottlieb, R. S. Pawell, *Sci. Rep.* **2019**, *9*, 3214.
- [53] H. Chen, J.-C. Meiners, *Appl. Phys. Lett.* **2004**, *84*, 2193.
- [54] S. Sivashankar, S. Agambayev, Y. Mashraei, E. Q. Li, S. T. Thoroddsen, K. N. Salama, *Biomicrofluidics* **2016**, *10*, 034120.
- [55] S. Shen, C. Tian, T. Li, J. Xu, S. W. Chen, Q. Tu, M. Yuan, W. Liu, J. Wang, *Lab Chip* **2017**, *17*, 3578.



- [56] A. S. W. Ng, W. L. W. Hau, Y.-K. Lee, Y. Zohar, *J. Micromech. Microeng.* **2004**, *14*, 247.
- [57] A. D. Stroock, M. Weck, D. T. Chiu, W. T. S. Huck, P. J. A. Kenis, R. F. Ismagilov, G. M. Whitesides, *Phys. Rev. Lett.* **2000**, *84*, 3314.
- [58] A. Minerick, A. Ostafin, H.-C. Chang, *Electrophoresis* **2002**, *23*, 2165.
- [59] S. Thamida, H.-C. Chang, *Phys. Fluids* **2002**, *14*, 4315.
- [60] P. Takhistov, K. Duginova, H.-C. Chang, *J. Colloid Interface Sci.* **2003**, *263*, 133.
- [61] N. Mishchuk, P. Takhistov, *Colloid Surf., A* **1995**, *95*, 119.
- [62] Y. Ben, H.-C. Chang, *J. Fluid Mech.* **2002**, *461*, 229.
- [63] I. Rubinstein, B. Zaltzman, *Phys. Rev. E* **2000**, *62*, 2238.
- [64] S. M. Rubinstein, G. Manukyan, A. Staicu, I. Rubinstein, B. Zaltzman, R. G. H. Lammertink, F. Mugele, M. Wessling, *Phys. Rev. Lett.* **2008**, *101*, 236101.
- [65] G. Yossifon, H.-C. Chang, *Phys. Rev. Lett.* **2008**, *101*, 254501.
- [66] T. Squires, M. Bazant, *J. Fluid Mech.* **2004**, *509*, 217.
- [67] A. González, A. Ramos, N. Green, A. Castellanos, H. Morgan, *Phys. Rev. E* **2000**, *61*, 4019.
- [68] Y. Ben, H.-C. Chang, in *The MEMS Handbook, MEMS: Applications* (Ed: M. Gad-el-Hak), Vol. 3, CRC Press, Boca Raton, FL **2005**.
- [69] Z. Gagnon, H.-C. Chang, *Electrophoresis* **2005**, *26*, 3725.
- [70] H.-Y. Lin, L.-C. Tsai, P.-Y. Chi, C.-D. Chen, *Nanotechnology* **2005**, *16*, 2738.
- [71] D. Lastochkin, R. Zhou, P. Wang, Y. Ben, H.-C. Chang, *J. Appl. Phys.* **2004**, *96*, 1730.
- [72] J. Wu, Y. Ben, D. Battigelli, H.-C. Chang, *Ind. Eng. Chem. Res.* **2005**, *44*, 2815.
- [73] G. Kunti, A. Bhattacharya, S. Chakraborty, *Electrophoresis* **2017**, *38*, 1310.
- [74] G. Kunti, A. Bhattacharya, S. Chakraborty, *J. Non-Newtonian Fluid Mech.* **2017**, *247*, 123.
- [75] G. Kunti, J. Dhar, S. Bandyopadhyay, A. Bhattacharya, S. Chakraborty, *Appl. Phys. Lett.* **2018**, *113*, 124103.
- [76] J. Meng, S. Li, J. Li, C. Yu, C. Wei, S. Dai, *J. Micromech. Microeng.* **2018**, *28*, 065004.
- [77] M. Nakano, H. Kurita, J. Komatsu, A. Mizuno, S. Katsura, *Appl. Phys. Lett.* **2006**, *89*, 133901.
- [78] A. Kumar, S. J. Williams, S. T. Wereley, *Microfluid. Nanofluid.* **2009**, *6*, 637.
- [79] C. Park, S. T. Wereley, *Lab Chip* **2013**, *13*, 1289.
- [80] J.-S. Kwon, S. P. Ravindranath, A. Kumar, J. Irudayaraj, S. T. Wereley, *Lab Chip* **2012**, *23*, 4955.
- [81] Y.-L. Chen, H.-R. Jiang, *Biomicrofluidics* **2017**, *11*, 034102.
- [82] G. Kunti, J. Dhar, A. Bhattacharya, S. Chakraborty, *Biomicrofluidics* **2019**, *13*, 014113.
- [83] L. Y. Yeo, D. Hou, S. Maheshwari, H.-C. Chang, *Appl. Phys. Lett.* **2006**, *88*, 233512.
- [84] L. Y. Yeo, J. R. Friend, D. R. Arifin, *Appl. Phys. Lett.* **2006**, *89*, 103516.
- [85] J. J. Qin, L. Y. Yeo, J. R. Friend, *Microfluid. Nanofluid.* **2009**, *8*, 231.
- [86] D. R. Arifin, L. Y. Yeo, J. R. Friend, *Biomicrofluidics* **2007**, *1*, 014103.
- [87] D. Hou, S. Maheshwari, H.-C. Chang, *Biomicrofluidics* **2007**, *1*, 014106.
- [88] D. Mampallil, D. Tiwari, D. van den Ende, F. Mugele, *Biomicrofluidics* **2013**, *7*, 044102.
- [89] G. W. Gale, A. A. Busnaina, *Part. Sci. Technol.* **1995**, *13*, 197.
- [90] C. C. Coussios, R. A. Roy, *Annu. Rev. Fluid Mech.* **2008**, *40*, 395.
- [91] S. Bhatnagar, H. Schiffer, C.-C. Coussios, *J. Pharm. Sci.* **2014**, *103*, 1903.
- [92] K. Petkovic-Duran, R. Manasseh, Y. Zhu, A. Ooi, *Biotechniques* **2009**, *47*, 827.
- [93] S. Oberti, A. Neild, T. W. Ng, *Lab Chip* **2009**, *9*, 1435.
- [94] D. Ahmed, X. Mao, J. Shi, B. K. Juluri, T. J. Huang, *Lab Chip* **2009**, *9*, 2738.
- [95] C. Wang, S. V. Jalikop, S. Hilgenfeldt, *Biomicrofluidics* **2012**, *6*, 012801.
- [96] P. Rogers, A. Neild, *Lab Chip* **2011**, *11*, 3710.
- [97] Y. Xie, D. Ahmed, M. I. Lapsley, M. Lu, S. Li, T. J. Huang, *J. Lab. Autom.* **2014**, *19*, 137.
- [98] Y. Xie, N. Nama, P. Li, Z. Mao, P.-H. Huang, C. Zhao, F. Costanzo, T. J. Huang, *Small* **2016**, *12*, 902.
- [99] D. Ahmed, M. Lu, A. Nourhani, P. E. Lammert, Z. Stratton, H. S. Muddana, V. H. Crespi, T. J. Huang, *Sci. Rep.* **2015**, *5*, 9744.
- [100] O. Fuchiwaki, Y. Tanaka, H. Notsu, T. Hyakutake, *Microfluid. Nanofluid.* **2018**, *22*, 80.
- [101] Y.-S. Liou, X.-J. Kang, W.-H. Tien, *Small* **2019**, *15*, 1804421.
- [102] M. Kaynak, A. Ozcelik, N. Nama, A. Nourhani, P. E. Lammert, V. H. Crespi, T. J. Huang, *Lab Chip* **2016**, *16*, 3532.
- [103] X. Lu, K. Zhao, H. Peng, H. Li, W. Liu, *Phys. Rev. Appl.* **2019**, *11*, 044064.
- [104] X. Liu, Q. Shi, Y. Lin, M. Kojima, Y. Mae, T. Fukuda, Q. Huang, T. Arai, *Exp. Therm. Fluid Sci.* **2019**, *106*, 78.
- [105] I. Iranmanesh, M. Ohlin, H. Ramachandriaiah, S. Ye, A. Russom, M. Wiklund, *Biomed. Microdevices* **2016**, *18*, 71.
- [106] H. V. Phan, T. Alan, A. Neild, *Anal. Chem.* **2016**, *88*, 5696.
- [107] M. Wiklund, R. Green, M. Ohlin, *Lab Chip* **2012**, *12*, 2438.
- [108] N. Garg, D. Boyle, A. Randall, A. Teng, J. Pablo, X. Liang, D. Camerini, A. P. Lee, *Lab Chip* **2019**, *19*, 1524.
- [109] Y. Kurashina, K. Takemura, J. Friend, *Lab Chip* **2017**, *17*, 876.
- [110] Y. Wang, Q. Zhang, Z. Zhu, F. Lin, J. Deng, G. Ku, S. Dong, S. Song, M. K. Alam, D. Liu, Z. Wang, J. Bao, *Sci. Adv.* **2017**, *3*, e1700555.
- [111] S. Yue, F. Lin, Q. Zhang, N. Epie, S. Dong, X. Shan, D. Liu, W.-K. Chu, Z. Wang, J. Bao, *Proc. Natl. Acad. Sci. USA* **2019**, *116*, 6580.
- [112] X. Shang, X. Huang, C. Yang, *Phys. Fluids* **2016**, *28*, 122001.
- [113] J. Lei, P. Glynn-Jones, M. Hill, *Lab Chip* **2013**, *13*, 2133.
- [114] A. R. Rezk, L. Y. Yeo, J. R. Friend, *Langmuir* **2014**, *30*, 11243.
- [115] G. Destgeer, B. Ha, J. Park, H. J. Sung, *Anal. Chem.* **2016**, *88*, 3976.
- [116] B. T. Hefner, P. L. Marston, *J. Acoust. Soc. Am.* **1999**, *106*, 3313.
- [117] A. Anhäuser, R. Wunenburger, E. Basselet, *Phys. Rev. Lett.* **2012**, *109*, 034301.
- [118] H. Li, J. R. Friend, L. Y. Yeo, *Biomed. Microdevices* **2007**, *9*, 647.
- [119] R. Shilton, M. K. Tan, L. Y. Yeo, J. R. Friend, *J. Appl. Phys.* **2008**, *104*, 014910.
- [120] R. V. Raghavan, J. R. Friend, L. Y. Yeo, *Microfluid. Nanofluid.* **2009**, *8*, 73.
- [121] P. R. Rogers, J. R. Friend, L. Y. Yeo, *Lab Chip* **2010**, *10*, 2979.
- [122] R. J. Shilton, M. Travaglini, F. Beltram, M. Cecchini, *Adv. Mater.* **2014**, *26*, 4941.
- [123] L. AlHasan, A. Qi, A. Al-Aboodi, A. Rezk, P. P. Y. Chan, C. Iliescu, L. Y. Yeo, *ACS Biomater. Sci. Eng.* **2016**, *2*, 1013.
- [124] G. Destgeer, H. Cho, B. H. Ha, J. H. Jung, J. Park, H. J. Sung, *Lab Chip* **2016**, *16*, 660.
- [125] G. Destgeer, J. H. Jung, J. Park, H. Ahmed, H. J. Sung, *Anal. Chem.* **2017**, *89*, 736.
- [126] H. Ahmed, A. R. Rezk, J. J. Richardson, L. K. Macreadie, R. Babarao, E. L. H. Mayes, L. Lee, L. Y. Yeo, *Nat. Commun.* **2019**, *10*, 2282.
- [127] F. Guo, Z. Mao, Y. Chen, Z. Xie, J. P. Lata, P. Li, L. Ren, J. Liu, J. Yang, M. Dao, S. Suresh, T. J. Huang, *Proc. Natl. Acad. Sci. USA* **2016**, *113*, 1522.
- [128] M. K. Tan, L. Y. Yeo, J. R. Friend, *EPL* **2009**, *87*, 47003.
- [129] A. Riaud, J.-L. Thomas, E. Charron, A. Bussonnière, O. B. Matar, M. Baudoin, *Phys. Rev. Appl.* **2015**, *4*, 034004.
- [130] A. Riaud, J.-L. Thomas, M. Baudoin, O. Bou Matar, *IEEE Trans. Ultrason., Ferroelectr., Freq. Control* **2016**, *63*, 1601.
- [131] M. Baudoin, J.-C. Gerbedoen, A. Riaud, O. B. Matar, N. Smagin, J.-L. Thomas, *Sci. Adv.* **2019**, *5*, eaav1967.

- [132] R. P. Hodgson, M. Tan, L. Yeo, J. Friend, *Appl. Phys. Lett.* **2009**, *94*, 024102.
- [133] K. S. Wong, L. Lee, Y. M. Hung, L. Y. Yeo, M. K. Tan, *Anal. Chem.* **2009**, <https://doi.org/10.1021/acs.analchem.9b02850>.
- [134] R. Wilson, J. Reboud, Y. Bourquin, S. L. Neale, Y. Zhang, J. M. Cooper, *Lab Chip* **2011**, *11*, 323.
- [135] J. Reboud, Y. Bourquin, R. Wilson, G. S. Palla, M. Jiwaji, A. R. Pitt, A. Graham, A. P. Waters, J. M. Cooper, *Proc. Natl. Acad. Sci. USA* **2012**, *109*, 15162.
- [136] Z. Mao, P. Li, M. Wu, H. Bachman, N. Mesyngier, X. Guo, S. Liu, F. Costanzo, T. J. Huang, *ACS Nano* **2017**, *11*, 603.
- [137] N. R. Glass, R. J. Shilton, P. P. Y. Chan, J. R. Friend, L. Y. Yeo, *Small* **2012**, *8*, 1881.
- [138] M. K. Tan, A. Siddiqi, L. Y. Yeo, *Sci. Rep.* **2017**, *7*, 6652.
- [139] A. R. Rezk, S. Ramesan, L. Y. Yeo, *Lab Chip* **2018**, *18*, 406.
- [140] A. R. Rezk, J. K. Tan, L. Y. Yeo, *Adv. Mater.* **2016**, *28*, 1970.
- [141] H. Bénard, *J. Phys. Theor. Appl.* **1901**, *37*, 254.
- [142] L. Rayleigh, *Philos. Mag.* **1916**, *32*, 529.
- [143] A. A. Darhuber, S. M. Troian, *Annu. Rev. Fluid Mech.* **2005**, *37*, 425.
- [144] H. Hu, R. G. Larson, *J. Phys. Chem. B* **2002**, *106*, 1334.
- [145] D. Brutin, V. Starov, *Chem. Soc. Rev.* **2018**, *47*, 558.
- [146] K. F. Lei, W. J. Li, *J. Lab. Autom.* **2008**, *13*, 227.
- [147] R. T. Tjeung, M. S. Hughes, L. Y. Yeo, J. R. Friend, *Appl. Phys. Lett.* **2011**, *99*, 214101.
- [148] R. J. Shilton, N. R. Glass, P. Chan, L. Y. Yeo, J. R. Friend, *Appl. Phys. Lett.* **2011**, *98*, 254103.
- [149] M. Geissler, B. Voisin, T. Veres, *Lab Chip* **2011**, *11*, 1717.
- [150] E. Asmolov, *J. Fluid Mech.* **2017**, *381*, 63.
- [151] E. Loth, A. J. Dorgan, *Environ. Fluid Mech.* **2009**, *9*, 187.
- [152] Marcos, R. Stocker, *Limnol. Oceanogr.: Methods* **2006**, *4*, 392.
- [153] H. Haddadi, H. Naghsh-Nilchi, D. Di Carlo, *Biomicrofluidics* **2018**, *12*, 014112.
- [154] W. R. Dean, S. Chapman, *J. Fluid Mech.* **1974**, *64*, 111.
- [155] J. Sun, Y. Li, F. Yan, C. Liu, Y. Sang, F. Tian, Q. Feng, P. Duan, L. Zhang, X. Shi, B. Ding, M. Liu, *Nat. Commun.* **2018**, *9*, 2599.
- [156] W. R. Dean, S. Chapman, *Proc. R. Soc. London, Ser. A* **1928**, *121*, 402.
- [157] S. A. Berger, L. Talbot, L. S. Yao, *Annu. Rev. Fluid Mech.* **1983**, *15*, 461.
- [158] G. H. McKinley, P. Pakdel, A. Öztekin, *J. Non-Newtonian Fluid Mech.* **1996**, *67*, 19.
- [159] E. Shaqfeh, *Annu. Rev. Fluid Mech.* **1996**, *28*, 129.
- [160] A. D. Stroock, S. K. W. Dertinger, A. Ajdari, I. Mezić, H. A. Stone, G. M. Whitesides, *Science* **2002**, *295*, 647.
- [161] S. L. Stott, C.-H. Hsu, D. I. Tsukrov, M. Yu, D. T. Miyamoto, B. A. Waltman, S. M. Rothenberg, A. M. Shah, M. E. Smas, G. K. Korir, F. P. Floyd Jr., A. J. Gilmand, J. B. Lord, D. Winokur, S. Springer, D. Irimia, S. Nagrath, L. V. Sequist, R. J. Lee, K. J. Isselbacher, S. Maheswaran, D. A. Haber, M. Toner, *Proc. Natl. Acad. Sci. USA* **2010**, *107*, 18392.
- [162] H.-C. Chang, L. Y. Yeo, *Electrokinetically Driven Microfluidics and Nanofluidics*, Cambridge University, Cambridge **2010**.
- [163] W. L. W. Hau, D. W. Trau, N. J. Sucher, M. Wong, Y. Zohar, *J. Micromech. Microeng.* **2003**, *13*, 272.
- [164] T. M. Squires, S. R. Quake, *Rev. Mod. Phys.* **2005**, *77*, 977.
- [165] G. Yossifon, I. Frankel, T. Miloh, *Phys. Fluids* **2006**, *18*, 117108.
- [166] H.-C. Chang, *Can. J. Chem. Eng.* **2006**, *84*, 1.
- [167] Y. Ben, E. Demekhin, H.-C. Chang, *J. Colloid Interface Sci.* **2004**, *276*, 483.
- [168] H.-C. Chang, G. Yossifon, E. A. Demekhin, *Annu. Rev. Fluid Mech.* **2012**, *44*, 401.
- [169] D. Hou, H.-C. Chang, *Phys. Fluids* **2006**, *18*, 071702.
- [170] S.-J. Liu, H.-H. Wei, S.-H. Hwang, H.-C. Chang, *Phys. Rev. E* **2010**, *82*, 026308.
- [171] G. Lippmann, *Ann. Chem. Phys.* **1875**, *5*, 494.
- [172] F. Mugele, J.-C. Baret, *J. Phys.: Condens. Matter* **2005**, *17*, R705.
- [173] L. Rayleigh, *Philos. Trans. R. Soc. London* **1884**, *175*, 1.
- [174] W. L. Nyborg, *J. Acoust. Soc. Am.* **1958**, *30*, 329.
- [175] J. Lighthill, *J. Sound Vib.* **1978**, *61*, 391.
- [176] N. Riley, *Annu. Rev. Fluid Mech.* **2001**, *33*, 43.
- [177] N. Riley, *IMA J. Appl. Math.* **1967**, *3*, 419.
- [178] J. Jalal, T. S. H. Leong, *Fluids* **2018**, *3*, 93.
- [179] L. A. Crum, *J. Acoust. Soc. Am.* **1980**, *68*, 203.
- [180] M. Minnaert, *Philos. Mag.* **1933**, *16*, 235.
- [181] M. S. Plesset, A. Prosperetti, *Annu. Rev. Fluid Mech.* **1977**, *9*, 145.
- [182] R. E. Apfel, C. K. Holland, *Ultrasound Med. Biol.* **1991**, *17*, 179.
- [183] J. Wu, G. Du, *J. Acoust. Soc. Am.* **1997**, *101*, 1899.
- [184] P. Tho, R. Manasseh, A. Ooi, *J. Fluid Mech.* **2007**, *576*, 191.
- [185] A. Volk, C. J. Kähler, *Phys. Rev. Appl.* **2018**, *9*, 054015.
- [186] O. Manor, L. Y. Yeo, J. R. Friend, *J. Fluid Mech.* **2012**, *707*, 482.
- [187] J. Lei, P. Glynne-Jones, M. Hill, *Phys. Fluids* **2016**, *28*, 012004.
- [188] J. Lei, M. Hill, C. P. de León Albarrán, P. Glynne-Jones, *Microfluid. Nanofluid.* **2018**, *22*, 140.
- [189] J. Lei, M. Hill, P. Glynne-Jones, *Phys. Rev. Appl.* **2017**, *8*, 014018.
- [190] O. Manor, A. R. Rezk, J. R. Friend, L. Y. Yeo, *Phys. Rev. E* **2015**, *91*, 053015.
- [191] A. Riaud, M. Baudoin, O. B. Matar, J.-L. Thomas, P. Brunet, *J. Fluid Mech.* **2017**, *821*, 384.
- [192] C. Eckart, *Phys. Rev.* **1948**, *73*, 68.
- [193] W. L. Nyborg, in *Physical Acoustics: Principles and Methods* (Eds: W. P. Mason, R. N. Thurston), Vol. II B, Academic Press, San Diego, CA **1965**.
- [194] C. Bradley, *J. Acoust. Soc. Am.* **1996**, *100*, 1399.
- [195] J. Friend, L. Y. Yeo, *Rev. Mod. Phys.* **2011**, *83*, 647.
- [196] L. Y. Yeo, J. R. Friend, *Biomicrofluidics* **2009**, *3*, 012002.
- [197] X. Ding, P. Li, S.-C. S. Lin, Z. S. Stratton, N. Nama, F. Guo, D. Slotcavage, X. Mao, J. Shi, F. Costanzo, T. J. Huang, *Lab Chip* **2013**, *13*, 3626.
- [198] L. Y. Yeo, J. R. Friend, *Annu. Rev. Fluid Mech.* **2014**, *46*, 379.
- [199] G. Destgeer, H. J. Sung, *Lab Chip* **2015**, *15*, 2722.
- [200] A. R. Rezk, O. Manor, J. R. Friend, L. Y. Yeo, *Nat. Commun.* **2012**, *3*, 1167.
- [201] A. R. Rezk, O. Manor, L. Y. Yeo, J. R. Friend, *Proc. R. Soc. A* **2014**, *470*, 20130765.
- [202] X. Y. Du, M. E. Swanwick, Y. Q. Fu, J. K. Luo, A. J. Flewitt, D. S. Lee, S. Maeng, W. I. Milne, *J. Micromech. Microeng.* **2009**, *19*, 035016.
- [203] J. Vanneste, O. Buhler, *Proc. R. Soc. A* **2011**, *467*, 1779.
- [204] M. B. Dentry, L. Y. Yeo, J. R. Friend, *Phys. Rev. E* **2014**, *89*, 013203.
- [205] M. K. Tan, L. Y. Yeo, *Phys. Rev. Fluids* **2018**, *3*, 044202.
- [206] A. A. Doinikov, P. Thibault, P. Marmottant, *Phys. Rev. E* **2017**, *96*, 013101.
- [207] T.-D. Luong, V.-N. Phan, N.-T. Nguyen, *Microfluid. Nanofluid.* **2011**, *10*, 619.
- [208] G. Destgeer, S. Im, B. H. Ha, J. H. Jung, M. A. Ansari, H. J. Sung, *Appl. Phys. Lett.* **2014**, *104*, 023506.
- [209] D. J. Collins, Z. Ma, Y. Ai, *Anal. Chem.* **2016**, *88*, 5513.
- [210] D. J. Collins, B. L. Khoo, Z. Ma, A. Winkler, R. Weser, H. Schmidt, J. Han, Y. Ai, *Lab Chip* **2017**, *17*, 1769.
- [211] T. Frommelt, M. Kostur, M. Wenzel-Schäfer, P. Talkner, P. Hänggi, A. Wixforth, *Phys. Rev. Lett.* **2008**, *100*, 034502.
- [212] R. J. Shilton, L. Y. Yeo, J. R. Friend, *Sens. Actuators, B* **2011**, *160*, 1565.
- [213] A. M. Gracioso Martins, N. R. Glass, S. Harrison, A. R. Rezk, N. A. Porter, P. D. Carpenter, J. Du Plessis, J. R. Friend, L. Y. Yeo, *Anal. Chem.* **2014**, *86*, 10812.
- [214] A. Sudeepthi, A. K. Sen, L. Yeo, *Microfluid. Nanofluid.* **2019**, *23*, 76.
- [215] Y. Q. Fu, J. K. Luo, N.-T. Nguyen, A. J. Walton, A. J. Flewitt, X. T. Zu, Y. Li, G. McHale, A. Matthews, E. Iborra, H. Du, W. I. Milne, *Prog. Mater. Sci.* **2017**, *89*, 31.

- [216] W. Cui, H. Zhang, H. Zhang, Y. Yang, M. He, H. Qu, W. Pang, D. Zhang, X. Duan, *Appl. Phys. Lett.* **2016**, *109*, 253503.
- [217] H. Zhang, Z. Tang, Z. Wang, S. Pan, Z. Han, C. Sun, M. Zhang, X. Duan, W. Pang, *Phys. Rev. Appl.* **2018**, *9*, 064011.
- [218] W. Cui, M. He, Y. Yang, H. Zhang, W. Pang, X. Duan, *Part. Part. Syst. Character.* **2018**, *35*, 1800068.
- [219] W. Liu, S. Pan, H. Zhang, Z. Tang, J. Liang, Y. Wang, M. Zhang, X. Hu, W. Pang, X. Duan, *ACS Cent. Sci.* **2018**, *4*, 899.
- [220] Z. Zhang, Z. Tang, W. Liu, H. Zhang, Y. Lu, Y. Wang, W. Pang, H. Zhang, X. Duan, *Micromachines* **2016**, *7*, 194.
- [221] X. Y. Du, Y. Q. Fu, S. C. Tan, J. K. Luo, A. J. Flewitt, W. I. Milne, D. S. Lee, N. M. Park, J. Park, Y. J. Choi, S. H. Kim, S. Maeng, *Appl. Phys. Lett.* **2008**, *93*, 094105.
- [222] Y. Q. Fu, L. Garcia-Gancedo, H. F. Pang, S. Porro, Y. W. Gu, J. K. Luo, X. T. Zu, F. Placido, J. I. B. Wilson, A. J. Flewitt, W. I. Milne, *Biomicrofluidics* **2012**, *6*, 024105.
- [223] H. Jin, J. Zhou, X. He, W. Wang, H. Guo, S. Dong, D. Wang, Y. Xu, J. Geng, J. K. Luo, W. I. Milne, *Sci. Rep.* **2013**, *3*, 2140.
- [224] J. Zhou, H. F. Pang, L. Garcia-Gancedo, E. Iborra, M. Clement, M. De Miguel-Ramos, H. Jin, J. K. Luo, S. Smith, S. R. Dong, D. M. Wang, Y. Q. Fu, *Microfluid. Nanofluid.* **2014**, *18*, 537.
- [225] J. Zhou, M. DeMiguel-Ramos, L. Garcia-Gancedo, E. Iborra, J. Olivares, H. Jin, J. K. Luo, A. S. Elhady, S. R. Dong, D. M. Wang, Y. Q. Fu, *Sens. Actuators, B* **2014**, *202*, 984.
- [226] N. G. Green, A. Ramos, A. González, A. Castellanos, H. Morgan, *J. Electrostat.* **2001**, *53*, 71.
- [227] A. M. Streets, Y. Huang, *Biomicrofluidics* **2013**, *7*, 011302.